Experimental Study of the Influence of Vegetation on Longitudinal Dispersion

by

Christophe Georges Mugnier

Diplôme d'ingénieur
Ecole Centrale Paris, 1995

Submitted to the Department of Civil and Environmental Engineering
in partial fulfillment of the requirements for the degree of

Master of Science in Civil and Environmental Engineering

at the

MASSACHUSETTS INSTITUTE OF TECHNOLOGY

June 1995

Author .....
Department of Civil and Environmental Engineering
June 29, 1995

Certified by.. .....
Heidi M. Nepf
Assistant Professor
Thesis Supervisor

Accepted by .....
Joseph Sussman
Chairman, Departmental Committee on Graduate Studies

Experimental Study of the Influence of Vegetation on Longitudinal Dispersion

by

Christophe Georges Mugnier

Submitted to the Department of Civil and Environmental Engineering
on June 29, 1995, in partial fulfillment of the
requirements for the degree of
Master of Science in Civil and Environmental Engineering

Abstract

Understanding the dispersion processes within marshes is important to assess their filtering abilities and their ecological limits.

A laboratory experiment was designed to study the influence of marsh vegetation on longitudinal dispersion. The flow through vegetation was modeled by a recirculating current going through an array of wooden dowels in a 24 m long flume.

The longitudinal dispersion coefficient K was estimated by releasing dye upstream of the array and measuring time series of concentration downstream of the array. The study included flow velocities ranging from 3 to 8 $cm.s^{-1}$ and dowel densities ranging from 0.5% to 5%. Within the accuracy of our estimation, the observed longitudinal dispersion coefficient did not vary significantly for the range of flow velocity and dowel density used in this study.

The shape of the concentration curves also demonstrated the existence of a delay phenomenon that affected 20% to 30% of a slug mass forming a 1 m long tail. This tail was attributed to the backflow region behind each dowel which trapped the dye and released it after some delay. A simple numerical model confirmed that delay zones, such as the backflow regions, can substantially increase the global longitudinal dispersion process.

Finally, an estimate of each dispersive process likely to occur in the experiments showed that shear flow dispersion due to the bed shear is the other dominant process. Because of enhanced diffusivity this process is diminished within the dowel array. This could explain why K does not dramatically increase through the vegetation.

Thesis Supervisor: Heidi M. Nepf
Title: Assistant Professor

Acknowledgments

It is my pleasant duty to acknowledge the financial support of the Fondation Georges Besse and the Fondation Jean Gaillard.

I am grateful to my advisor Heidi Nepf for her enthusiasm and for guiding my first steps in a lab.
I also want to thank my brother and my mother for believing in me and encouraging me.
Special thanks to Robert for his friendship and reminding me when to take a break.
Finally, all my thougths to Stéphanie for her love and epistolary support.

Contents

List of Figures

List of Tables

Chapter 1

Introduction

1.1 Relevance of the Project

At least 37 percent of the U.S population is located in counties adjacent to the oceans or to major estuaries. The wastes from this population and its associated activities (septic waste, pesticides, and fertilizers) contribute to the deterioration of ocean and coastal waters [14].

Chemical, biological, and physical processes determine the fate and transport of wastewaters to coastal waters. Mathematical and conceptual models are used extensively to explain processes that disperse the water-borne substances and modify the water quality. Using these models, the limits on waste discharges can be assessed and management plans for pollution control in coastal regions can be designed. Among the many different types of coastal environments that can been studied, marshes have recently begun receiving increased attention due to their surprising ability to improve water quality. Marshes are a type of wetlands common at the mouth of rivers and can be considered as transition zones between land and ocean. The photosynthetic potential of their vegetation and the abundance of nutrients continually flushed from upland regions make marshes among the most productive areas on earth. Marshes are usually covered with low-growing emergent vegetation. Along the Eastern seaboard, for example, marshes are dominated by salt-tolerant herbaceous plants, notably cordgrass (*Spartina alterniflora*). In addition to their vegetative productivity, marshes are

a favorable habitat for zooplanktons, worms, insects, fishes, and birds, all feeding on plants or on one another. Therefore, marshes constitute a very complex and sensitive ecosystem which provides communication between terrestrial and aquatic environments. In addition, marshes stabilize shorelines by tempering the effects of high tides and providing natural flood control systems. Finally, coastal marshes affect coastal water quality by acting as huge filters and buffers for land-source pollutants. This is perhaps the most important, though less understood, function of marshes, i.e. they provide free treatment for many types of water pollution through chemical, biological, and physical processes. Chemical reactions and biological decomposition breakdown complex compounds into simple substances. Through absorption, plants remove excess nutrients for biomass production and in return produce oxygen, leading to a more complete bacterial decomposition of pollutants. Physical processes such as the small-scale hydrodynamics associated with flow obstruction enhance the spreading of the plumes of pollutants and decrease critical concentrations of nutrients and contaminants.

A study focusing on the hydrodynamics of these complex ecosystems could help to explain how marshes filter and buffer land-source fluxes. Specifically, the purpose of the present work is to understand the influence of marsh vegetation on longitudinal dispersion processes. A better understanding of this process would eventually result in a better assessement of the ecological limits of marshes, as their recycling and dispersive power is not boundless, and in a better design of constructed wetlands [13] which could provide a relatively simple and inexpensive solution for controlling many water pollution problems without affecting natural wetlands.

1.2 Scope of the Project

The influence of vegetation on longitudinal dispersion was studied experimentally in a flume. The plants were modeled by an array of wooden dowels. Three flow velocities and three plant densities in addition to the no-plant case were examined. Rhodamine was injected continuously upstream of the dowel array and sampled downstream.

The dispersion coefficient was estimated from the concentration time series at the downstream station.

The analysis of the results eventually helped us assess which mechanisms control the longitudinal dispersion process through a vegetation and how.

1.3 Organization of the Thesis

Chapter 2 (page 12) gives the definition of dispersion and lists the most common results about shear flow dispersion, before expanding to more recent studies about "dead-zones" and their effect on longitudinal dispersion.

Chapter 3 (page 18) describes the experimental devices and the set-up of the experiments.

Chapter 4 (page 26) discusses the various diffusive and dispersive effects likely to account for longitudinal dispersion in our modeled vegetation. It examines the backflow region behind each dowel, pictures the resulting delaying effect (page 29), and theoretically presents how the relative importance of shear flow dispersion in the wake of the dowels (page 32) can be parameterized. Then it recalls the main dipersion-governing equations and their limitations (page 35), before explaining how the longitudinal dispersion coefficient K was actually estimated from experimental time-concentration curves (page 37).

Chapter 5 (page 40) presents and discusses the estimates of K we obtained for each density and flow velocity. It assesses the influence of the backflow region with a simple numerical model, and estimates the magnitude of mechanical dispersion, of shear flow dispersion in the wakes of the dowels and of shear flow dispersion due to the bed. Then it concludes which effects actually govern the dispersion process inside the vegetation.

Experimental curves are given in appendices A and B (page 65 and 68). The listing of the numerical model is given in appendix C (page 78).

Chapter 2

Literature Review

Dispersion is the hydraulic process by which the concentration of a substance released in a watercourse is leveled. Longitudinal dispersion is important only when longitudinal gradients exist in the concentration field. This is the case, for example, if a spill of hazardous material occurs in a river. Dispersion results from turbulent mixing in the flow, and from shear effects due to non-uniform velocity profiles. The former can be modeled by Fickian diffusion equations using a turbulent diffusion coefficient. The latter were first studied by Taylor [22], who gave a model of the spreading of dissolved contaminants through a pipe. The non-uniformity of the velocity profile in a cross-section of the pipe combines with molecular diffusion : the former stretches the contaminant cloud and therefore enhances dispersion, while the latter reduces cross-sectional concentration gradients and therefore lessens the consequences of the former. Figure 2-1 pictures this process. After an initial period, a balance is reached between these two effects, where the contaminant cloud grows linearly with time. A model analogous to the one-dimensional diffusion process was proposed by Taylor. Its equation, known as the "one-dimensional dispersion equation", can be written :

$$\frac{\partial \bar{C}}{\partial t} + \bar{u}\frac{\partial \bar{C}}{\partial x} = K\frac{\partial^2 \bar{C}}{\partial x^2}, \tag{2.1}$$

where $\bar{C}$ and $\bar{u}$ are respectively the concentration of contaminant and the flow velocity averaged over the cross-section of the pipe, and K the "longitudinal dispersion

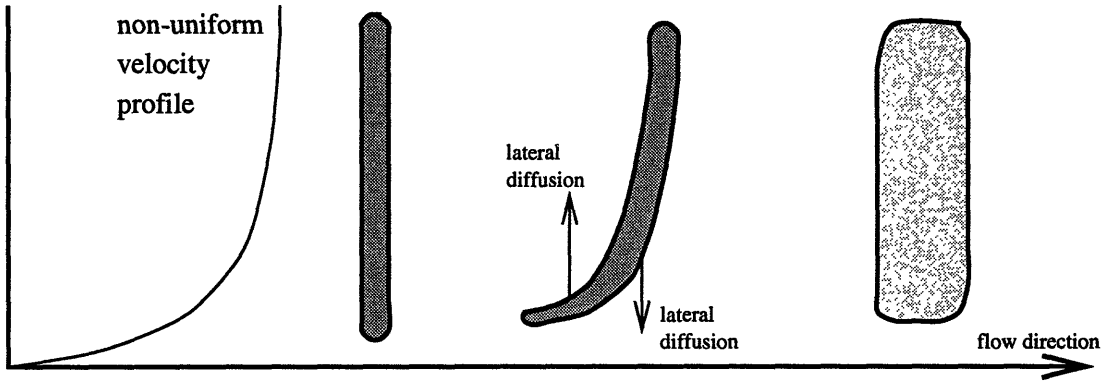

Figure 2-1: Schematic of the Longitudinal Dispersion Process

coefficient." As equation 2.1 implies, K plays a role at the cross-section scale that is similar to the role played by the molecular diffusion D at a microscopic scale.

In the case of a laminar flow through a pipe and based on a parabolic velocity profile, Taylor's result is :

$$K = \frac{a^2 \bar{u}^2}{48D}, \tag{2.2}$$

where a is the radius of the pipe.

In the case of a turbulent flow through a pipe and based on an empirical velocity profile, Taylor's result is :

$$K = 10.1 a u^*, \tag{2.3}$$

where u^* is the shear flow velocity. These results are used in section 5.2.1 (on page 46).

Elder [4] applied Taylor's concept to flows moving down an infinitely wide plane, and considered the shear associated with the vertical profile of streamwise velocity. In this case K is given by :

$$K = -\frac{1}{d} \int_0^d u' \int_0^z \frac{1}{\epsilon d} \int_0^z u' d \, dz \, dz \, dz, \tag{2.4}$$

where d is the depth of the flow, ϵ is either the molecular diffusion coefficient D if the flow is laminar or the lateral turbulent diffusion coefficient ϵ_t which is a function of the vertical coordinate z if the flow is turbulent, and u' is the local deviation of the velocity from $\bar{u}$. A surprising result is that K is inversely proportional to ϵ. Introducing a logarithmic velocity profile in equation 2.4 and considering a turbulent flow, Elder's result is :

$$K = 5.93 d u^*. \tag{2.5}$$

Fischer [6] [7] [8] applied Taylor's theory to study longitudinal dispersion in rivers. Fischer concluded that the shear effects in real streams were mostly due to variations of the velocity across the width of the channel, and that Elder's analysis, which takes into account only the variations of the velocity across the depth of the channel, must be modified. Fischer's formula based on lateral variation in longitudinal velocity is

similar to equation 2.4 :

$$K = -\frac{1}{A}\int_0^W u'd \int_0^y \frac{1}{\epsilon_t}\int_0^y u'd\ dy\ dy\ dy, \tag{2.6}$$

where A is the cross-sectional area and W is the width. Here again, K is inversely proportional to the diffusion coefficient.

When they obtained their dispersion coefficients, Taylor, Elder, and Fischer assumed a Fickian, i.e. diffusion-like, dispersion process after some initial period. Equation 2.1 is then valid ; the longitudinal distribution of concentration corresponding to a slug release is a Gaussian, the variance of which $\sigma^2 = 4Kt$ grows linearly with time, and the maximum concentration decreases as $1/\sqrt{t}$. Fischer considered the initial time period to be W^2/ϵ_t.

Fischer also gave a "routing procedure" to estimate K in real streams. This method compares the observation at a downstream-point to the prediction based on the observation at an up-stream point. It was used by Nabil, Abd El-Hadi and Kersi [1] in their experimental study of longitudinal dispersion of flow over rough beds. Dye studies by Nordin and Sabol [16] showed that the variance of the distribution increased faster than linearly with time, that concentration distributions maintained an almost constant skewness coefficient and never became normal, which implied that Taylor's theory never strictly applied. Figure 2-2 pictures the skewness of an observed concentration distribution corresponding to a slug release.

Valentine and Wood [23] proposed a numerical model of "dead-zones" in order to explain the persistent skewness observed in field data. A "dead-zone" is a region of zero or low velocity. In their model, the "dead-zones" communicate with the flow zone only by molecular and turbulent diffusion, and the velocity profile is logarithmic. Contaminant is trapped in these zones and released after the passage of the main cloud. This creates a "tail" and increases the skewness of the concentration distribution. The authors concluded that, according to the results of their simulation, the presence of "dead-zones" still leads to a Fickian type dispersion process but, if compared to the no-dead zone model, dispersion is enhanced and the length of the

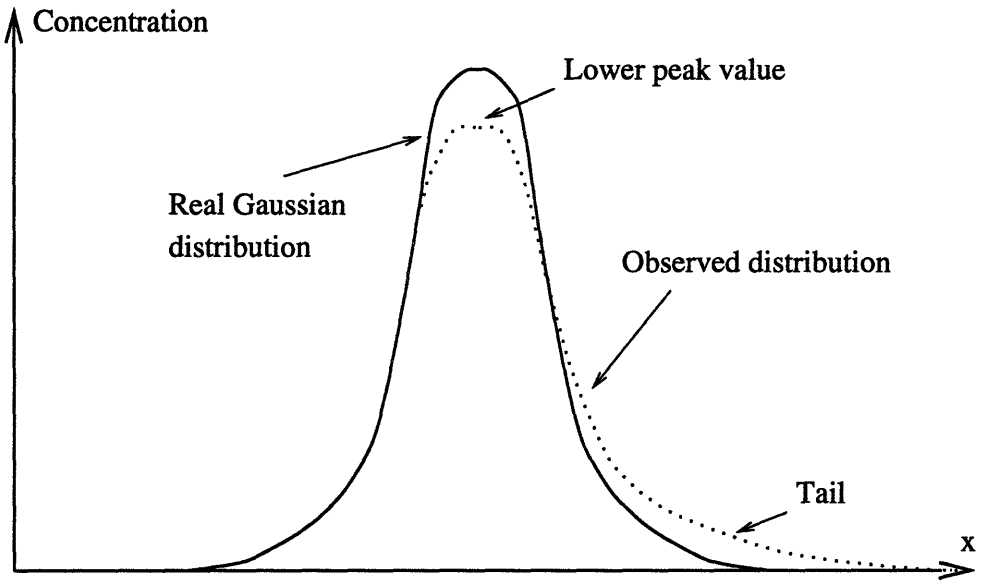

Figure 2-2: Skewness of Typically Observed Concentration Distributions

initial period is increased.

Field studies performeded by Nordin and Troutman [17] also demonstrated a persistent skewness in the concentration distribution and the presence of a long tail of dye upstream. Therefore, the distribution never became a Gaussian. Using a numerical model similar to that of Valentine, and estimating the parameters of the model with field data, predicted skewness values increased and fit the observed data much better. However, the authors pointed out that the "dead-zone" model leads to a rapidly decaying skewness coefficient, which is not confirmed by their field data.

Chikwendu and Ojiakor [2] used a slow-zone model instead of a dead-zone model to explain the skewness of the concentration distribution observed in real streams. They considered a slow moving zone near the bottom of the channel overtopped by a fast moving zone in the middle of the channel, each zone having a uniform velocity profile. They obtained analytical solutions explaining the presence of the tail by the combination of a large Gaussian distribution followed by a small Gaussian distribution traveling at a reduced velocity.

Legrand-Marcq and Laudelout [11] studied the influence of the flow rate on the volume of dead-zones in forest streams. They concluded that a decreasing flow rate

increases the dead volume and decreases the longitudinal dispersion. This apparently counter-intuitive result can be explained by the fact that when the dead volume fraction tends towards unity, which is possible in forest streams, there is no dispersion unless by molecular diffusion.

Yu [24] solved for the longitudinal dispersion using Laplace transform and numerical inversion the dead-zone model. Seo [19] experimentally and numerically examined longitudinal dispersion in natural streams under low flow conditions. He modeled the water bed with pool-riffle sequences. Therefore the flow conditions are not as idealized as in the previous models, and Seo's models allow recirculating flows behind obstacles. Seo's experiments as well as his numerical model agreed and demonstrated significantly skewed concentration distributions with long tails. Seo underlined the fact that recirculating flow results in a strong storage mechanism for water and tracer. Backflow regions are analogous to trapping zones which exist behind plant stems as explained further below.

The goal of the present research is to study the enhancement of longitudinal dispersion due to vegetation. Few articles have studied the influence of obstructions across the entire water depth on flow characteristics.

In her Master's thesis, Zavistoski [25] modeled a flow through vegetation using a pump-driven current going through wooden dowels in a laboratory flume. She studied the effects of flow obstruction by the dowels on the velocity and turbulence profiles within the obstructions. This work has concluded that increasing plant densities significantly increases the horizontal and vertical turbulence intensities, because of wake interactions creating strong lateral shears and pressure-forced vertical velocities that are swept from the wakes into the flow. Since increasing ϵ_t decreases K, longitudinal dispersion is expected to be enhanced from the effects of increasing turbulence intensities. Zavistoski also demonstrated the presence of backflow regions behind the dowels. These regions are similar to delay zones and are expected to enhance K.

Building upon this work and using the same experimental devices, the present research is a study of the change in dispersion due to the presence of vegetation.

Chapter 3

Experimental Devices and Set-up

3.1 Experimental Devices

3.1.1 Fluorometry Theory

The essence of fluorescence spectrometry, also called fluorometry, is that a molecular sample, illuminated by light from an external source, emits fluorescence at a different wavelength, generally longer than the exciting light. This process is instantaneous, as the time between excitation and emission is less than one nanosecond. The wavelength of the fluorescence is independant of the excitation wavelength, and its intensity depends on the intensity of the exciting light and on the concentration of the fluorescent substance in the sample. The relationship between the fluorescence intensity of a dilute sample and its concentration can be derived from the Beer Law of absorption. According to the Beer Law,

$$I_t = I_0 10^{-\varepsilon bc}, \tag{3.1}$$

where I_0 and I_t are the intensities of the incident and transmitted light beams, $\mathcal{E}$ is the molar absortivity ($mol^{-1}.cm^{-1}$) of the fluorescent substance, c is its molar concentration (mol), and b (cm) is the path length, i.e., the distance the incident

beam goes through the sample. The intensity absorbed, I_a, is given by

$$I_a = I_t - I_0 = I_0(1 - 10^{-\mathcal{E}bc}). \tag{3.2}$$

Only a fraction of photoexcited molecules lose their energy via this fluorescence mechanism. Let ϕ_f, also called the quantum yield, be this fraction. The intensity of the fluorescence I_f is then given by

$$I_f = I_0\phi_f(1 - 10^{-\mathcal{E}bc}) \simeq 2.303\ I_0\ \phi_f\ \mathcal{E}bc \tag{3.3}$$

when $\mathcal{E}bc \leq 0.05$ (then the error from the expansion is less than 5%). Therefore, $I_f\ \alpha\ I_0$ and $I_f\ \alpha\ c$. Fluorometric measurements are based on the measurement of the ratio I_f/I_0, but measurements are complicated by the presence of interfering fluorescent materials in the sample. Because of these interfering materials, I_0 and I_f tend to be overestimated. A solution to this problem is the addition of two filters to our fluorometric system. The exciting filter sets the wavelength of the exciting light to maximize the absorption by the substance under study and minimize the absorption by interfering materials. The emission filter passes the particular wavelength of the fluorescent light emitted by the material under study and stops any other light. Figure 3-1 summarizes the fluorometry technique.

The fluorometer manufactured by Turner used in our experiments is designed to make field measurements as low as 0.1 part per billion of rhodamine WT, which is more than enough for our lab experiments. The Turner fluorometer also makes it possible to get rid of interfering light, thanks to a BLANK button, and to expand the concentration scale, thanks to a SPAN button. As we were interested only in measuring relative concentrations, these buttons were used to optimize the recordings, with no further effect on the results.

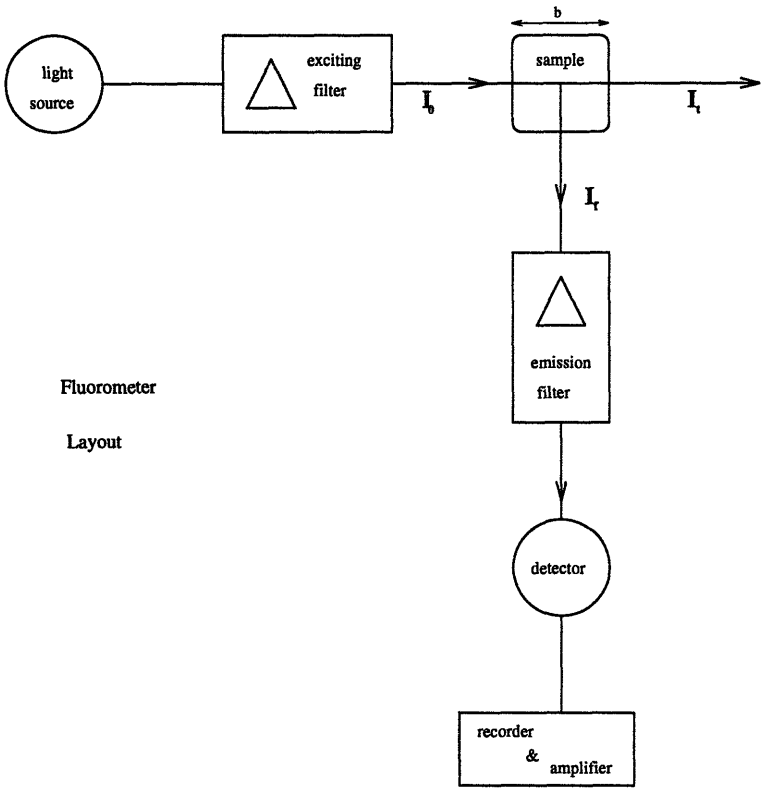

Figure 3-1: Basic Layout of a Fluorometer

3.1.2 Rhodamine

Rhodamine is an organic compound. Rhodamine WT is related to rhodamine B but, does not adsorbed to suspended sediments. It is a widely used tracer due to its high detectability.

The molecular diffusivity of Rhodamine in water was found from experimental data giving the Schmidt number $S_c = \nu_{water}/D$ of a diffusing substance as a function of the molecular weight of this substance. $D_{rhodamine}$ was found to be approximately $5 \times 10^{-6} cm^2.s^{-1}$. The diffusivity of Rhodamine is low because it is a very heavy molecule.

The concentration of injected Rhodamine was taken far above the detection threshold of the fluorometer, so that the advecting cloud of dye could be easily visualized. This was helpful in monitoring the extent of cross-sectional mixing.

3.1.3 Mariotte Bottle

The Mariotte bottle is a simple device used to perform continuous dye releases. It is also possible to use a pump, but the Mariotte bottle frees the experimenter from the burden of finding a source of energy, which is often a problem during field experiments.

Figure 3-2 depicts the device. A Mariotte bottle is simply a sealed tank, and the only entry of air is through the tube going through the stopper. Initially, P_{air} inside the bottle is equal to P_{atm}, and the initial water level inside the tube is equal to the initial water level inside the bottle. Immediately after the begining of the release, $v = \sqrt{2gh_i}$, from Bernouilli. As water is released from the bottle, P_{air} decreases, and the water level inside the tube where the pressure is still P_{atm} is lower than the water level inside the bottle, as shown in the first drawing of Figure 3-2. The gap between these two surfaces increases as P_{air} decreases. During this non-steady period, $v = \sqrt{2gh}$. Eventually, the water level inside the tube reaches the lower end of the tube, as it is shown in the second drawing of Figure 3-2, and a steady state occurs. It is characterized by a constant outflow velocity, $v = \sqrt{2gh_f}$, and therefore a constant outflow rate. The Mariotte bottle used in our experiments produced a constant flow

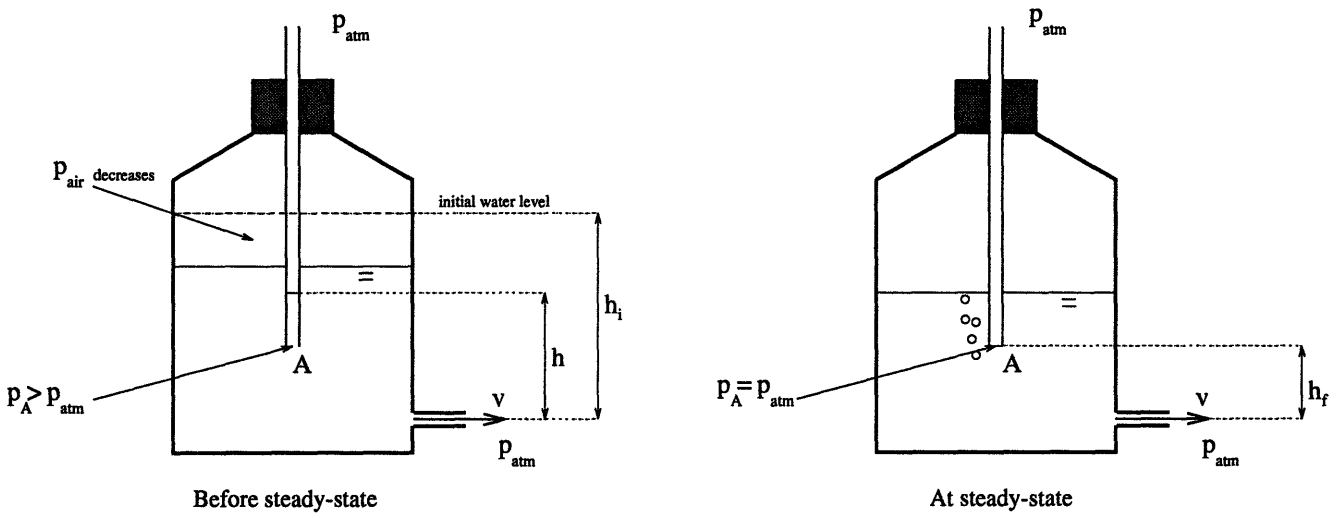

Figure 3-2: Basic Principle of a Mariotte Bottle

rates as low as 9 $cm^3.s^{-1}$.

3.2 Set-up

Our research builds upon Zavistoski's work which examined the effects of plant density on the velocity and turbulence structure. In her thesis, she described the enhancement of vertical and longitudinal turbulence intensities. We want her conclusions to help us understand the results of our laboratory study of longitudinal dispersion. In order to use quantitative results from Zavitoski, we have tried as much as possible to recreate the flow conditions she studied, and for that purpose, we conducted our experiments in the same flume, used the same type of dowels, and studied the same dowel densities.

The series of laboratory experiments were conducted at Parsons Lab, MIT, in a 24 m long, 38 cm wide and 60 cm high glass-walled flume. During our experiments, the flume was filled up to 20 cm. The velocity of the recirculating current was measured by a flow meter connected to the diaphragm valve controlling the flow. The resolution of the flow meter was 5 gpm. The mean velocity, $\bar{u}$ (cm/s), was readily calculated using the conversion $\bar{u} = 0.9\ q$, where q $(gpm \times 10)$ is read on the flow meter. The error on $\bar{u}$ was then 0.5 cm/s. Three velocities were selected. The

density	density (%)	n^0 of dowels per m^2	n^0 of dowels per board	S (cm)
low	0.5	154	72	8.0
medium	1.4	441	206	4.8
high	5.5	1700	795	2.4

Table 3.1: Densities of Dowels

low velocity corresponded roughly to $q = 3$, the medium to $q = 6$ and the high to $q = 9$. The only way to get an accurate estimate of $\bar{u}$ was to back-calculate it from the experimental curves. This is discussed later in section 4.5 on page 37.

Quarter-inch-diameter wooden dowels were used to model *Spartina alterniflora.* The dowel size was chosen based on actual stalk diameters listed in Gray's Manual of Botany [5]. Those dowels were drilled and glued on plexiglass boards. These boards were half an inch thick, 37 *cm* wide and 120 *cm* long. Four boards were built. Each dowel was approximately 22 *cm* long so that it would always protrude through the entire water column.

Dowel densities were chosen by Zavistoski based on a wake interaction criterion. The higher the density, the more extensive was the interaction between the individual wakes. The lowest density was set so that there was almost no interaction between individual wakes. The densities and the number of dowels used are listed in table 3.1. S is the average longitudinal spacing between the dowels.

Zavistoski designed a repeating pattern of dowels which incidentally created lateral surface oscillations at the medium and high densities. It was due to resonance between the vortex shedding from the dowels and the lateral standing wave. The uniform spacing of dowels promoted synchronous vortex shedding which promoted the resonance phenomenon. In order to avoid this phenomenon which could highly influence the dispersion process in our experiment, the dowels were randomly displaced. The length of the dowel array (480 *cm*) was such that even at the lowest density the flow was fully blocked when looking downstream. Unfortunately, at low density, even with the randomly positioned dowels the lateral seiching appeared after approximately 10 minutes. To avoid it, the pump was switched off after each trial

long enough to damp surface oscillations, and switched on again just before the next trial. As trials lasted less than 6 minutes, seiching never fully developed. The problem could also be avoided at medium density. But at high density the seiching developed after less than 45 s and was therefore acting during half of each trial.

A piece of rubberized coconut fiber was placed beneath the inlet to reduce turbulence and flow straighteners were placed 2 meters downstream of the inlet to avoid swirls and surface waves and to produce uniform flow conditions in the test section.

In order to minimize discontinuity at the bed a 50 cm long aluminum toe was added upstream of the first plexiglass board. The four plexiglass boards were aligned and fixed together using strong waterproof tape.

The release point was 400 cm downstream of the inlet, which was far enough not to affect the injection by the increased bottom shear created by the coconut fiber. The begining of the 480 cm long dowel array was 450 cm downstream of the release point. The recordings of dye concentration were done 30 cm downstream of the end of the array.

The idea was to give time for the dye to be well-mixed in the vertical and the lateral before entering the array. From the experimental values of u^* given by Zavistoski, and based on :

$$D_{t\ z} = \frac{1}{15}\ u^* h, \tag{3.4}$$

and

$$D_{t\ y} = 0.15\ u^* h, \tag{3.5}$$

we could estimate the values of the vertical and lateral diffusivities to be respectively 0.53 $cm^2.s^{-1}$ and 1.2 $cm^2.s^{-1}$. From section 4.4 (on page 35) we found that the minimum length to complete mixing in the vertical and the lateral was respectively 11 m and 18 m. Nevertheless visual observations showed that after 450 cm the dye appeared well mixed in the lateral and mixed in the upper half in the vertical. Complete vertical mixing was observed when the dye had gone 50 cm into the array.

For the no-dowel-case, one 15 cm long and one 50 cm long sections of dense

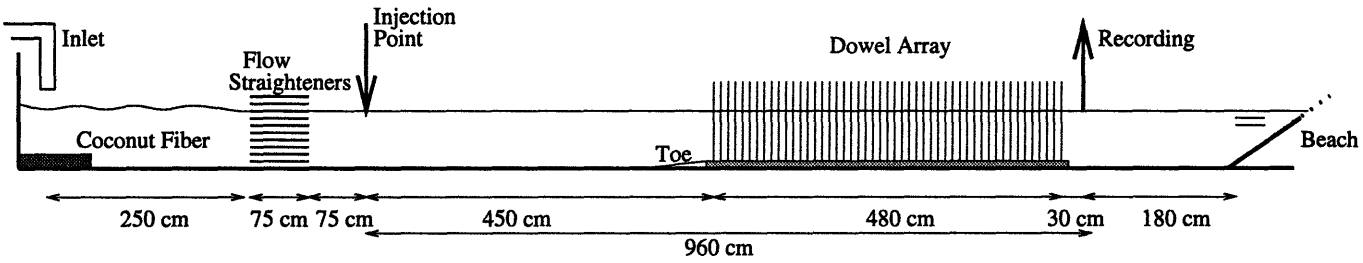

Figure 3-3: Flume Set-up

dowels were placed respectively 95 *cm* downstream of the injection point to force vertical mixing and 40 *cm* upstream the recording point to smooth the concentration records.

Chapter 4

Theory

4.1 Overview of Dispersion Effects

Dispersion is the hydraulic process by which a plume of contaminant spreads longitudinally and dilutes. Various complex effects contribute to dispersion. For example Taylor showed that in a pipe flow dispersion can result from turbulent diffusion combined with non-uniform advection due to velocity shear. The resulting enhanced longitudinal spreading is called **shear flow dispersion**. This was developed in chapter 2 (on page 12). Dispersion can also arise from differences in flow path. This dispersive effect called **mechanical dispersion** dominates in porous media flow for example. A final dispersive process can arise from the presence of **"dead-zones"**, or regions of comparative low or no velocity. Contaminants are temporarily trapped in these regions and re-released after some delay. Successive delays of some fraction of the plume effectively disperse the plume longitudinally. The present work studies the effect of surface-piercing plants on the various mechanisms of dispersion. The presence of obstructions across the entire water depth is expected to enhance spreading and mixing.

The following subsections list the diffusive and dispersive effects expected to appear in our experiments.

4.1.1 Turbulent Diffusion

Zavistoski showed that the dowel-obstructions used to model the plants enhance turbulent diffusion in the flow. She demonstrated that both horizontal and vertical turbulence intensities increase when the dowel density increases. It is no surprise that shear created by stems increases horizontal turbulence intensity. The increase in vertical turbulence intensity can be explained by the presence of pressure-driven vertical velocities in the near-dowel region upstream and downstream. When the horizontal turbulence intensity is high enough, horizontal velocity fluctuations can sweep the vertical velocities out of the near-dowel regions. As a consequence, swept vertical velocities increase the vertical fluctuations in the whole volume, and this in turn increases the vertical turbulent diffusion.

The spinning of horseshoe vortices created by the highly sheared flow at the bed interacting with the dowels can also account for the enhanced lateral and vertical turbulence intensities.

4.1.2 Dispersive Processes

The bed and the walls of the flume induce a non-uniform velocity profile in the vertical and the lateral. This can create shear flow dispersion if the shear has time to combine with turbulent diffusion described above.

Shear flow dispersion should also occur at the dowel scale because of the 40-60% reduction of the velocity in the dowels' wakes, compared to the average cross-sectional velocity. The time scale of this process is discussed in section 4.3.

Mechanical dispersion should also play a role due to the presence of frontal obstructions in the flow. This process is different from turbulent diffusion and shear flow dispersion, which both involve diffusion. The proof is that mechanical dispersion of solid can be experienced at creeping flow when the effective diffusivity of the particles is zero. Section 5.3.2 on page 56 pictures and parameterizes mechanical dispersion through a dowel array.

Finally, trapping effects due to the presence of a backflow region behind each

dowel which acts like a dead-zone can account for enhanced spreading through the vegetation. The characteristics of the backflow region are described further below.

4.1.3 Scope of the Analysis

All the processes described above are complex and their individual influence all the more difficult to predict since the processes interact with one another. The way turbulent diffusion combines with the non-uniformity of velocity profiles has already been emphazised. One should keep in mind that shear flow dispersion effects decrease with increasing cross-sectional diffusion. Therefore, two consequences of the presence of dowels, the increase of vertical turbulent diffusion and shear dispersion in the wake of the dowels, have opposite effects on the spreading through the vegetation.

The experiments described here cannot examine the various dispersion mechanisms individually. Instead, we consider that all the mechanisms combine so that the spreading of the cloud can be modeled by a one-dimensional Fickian equation parameterized by an "apparent" or "global" dispersion coefficient K that we are going to evaluate through a series of dye releases. When estimating this bulk dispersion coefficient, our assumption of a Fickian process can be checked. The order of magnitude of each of the different dispersion effects can be estimated using other models in order to assess which phenomenon influences the most the "global" dispersion (section 5.3).

Two scales of analysis, dowel scale and global scale, should be considered when studying K. The following processes are important at each scale. At the dowel scale, shear dispersion in the wakes, dead-zone effects and mechanical dispersion should be considered.

At a global scale, increase of turbulence intensity with increasing dowel density and bed or wall shear are considered. Effects at both scales contribute to the effective K parameter that can be observed through our dye experiments.

4.2 Main Features of the Flow Behind a Single Dowel

The characteristics of the wake downstream of a dowel depend on the Reynolds number $R_e = \bar{u}d/\nu$ where $\bar{u}$ is the mean flow velocity, d the dowel diameter and $\nu = 10^{-6}\ m^2.s^{-1}$ the water kinematic viscosity. This dependance has been widely studied by different techniques and five typical flow patterns can be found.

- At $R_e < 1$ viscous forces dominate and there is no separation downstream of the dowel. This pattern is called "creeping flow".
- At $R_e = o(10^1)$, a steady separation bubble can be noticed behind the dowel. This separation zone is due to a contrary pressure gradient behind the dowel.
- At $R_e = o(10^2)$, a oscillating vortex street called Karman vortex street is spread into the wake.
- At $R_e = o(10^4)$, the wake is turbulent but the boundary layer just downstream of the dowel is still laminar.
- At $R_e = o(10^6)$, the wake is turbulent, and the boundary layer downstream of the dowel is also turbulent. Therefore separation behind the dowel is delayed compared to the the previous case and the wake is narrower.

The limitation on the resolution of the flow velocity ($0.5\ cm.s^{-1}$) prevents us from choosing R_e lower than 30. Moreover, as the velocities used in our experiments are lower than $20\ cm.s^{-1}$, R_e is lower than 1200. Therefore only the second and the third patterns will be recognized in our experiments.

Kovasznay [10] measured the lateral profiles of the wake of a cylinder with a hot-wire anemometer. Gerrard [9] investigated wakes of cylinders and other bluff bodies by means of flow visualization. Both studies were strictly 2-D, i.e. they did not include the effect of vertical shear. However they covered a wide range of R_e values and the two authors gave interesting results about the transition between the steady

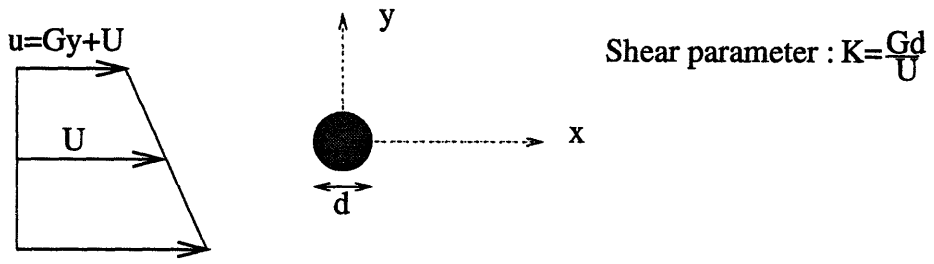

Figure 4-1: Definition of a Linear Shear Flow

separation bubble pattern and the vortex street pattern. According to Kovasznay the critical Reynolds number for vortex shedding is $R_{crit} = 40$.

Gerrard introduced two critical values R_{osc} and R_{vs}. Below R_{osc} the flow is steady and eddies in the separation bubble are standing eddies. The length of the bubble is approximately d. Gerrard observed that dye introduced inside the bubble cannot escape. As R_e gets closer to R_{osc}, the center line behind the bubble becomes wavy. Between R_{osc} and R_{vs} the wake **oscillates** but no **vortex shedding** is observed. Above R_{vs} eddies are spread into the wake and Gerrard observed that dye applied behind the separation points is shed into the wake. According to Gerrard, $R_{osc} = 34$ and R_{vs} can only be estimated between 55 and 60. The author also argues that $R_e = 100$ marks the end of the range in which there is any remnant of the standing eddies behind the dowel. Therefore trapping effects disappear at $R_e = 100$.

As the existence of trapping zones depends on R_e, we can expect longitudinal dispersion to also depend on R_e.

Studying the movement of dye behind a single dowel Zavistoski found values of R_{crit} between 360 and 380, i.e. ten times larger compared to Kovaznay's and Gerrard's result. This may be due to the finite length of the dowel. Or this could be an effect of the shear. The increase of R_{crit} in a linear shear flow was studied by Kiya, Tamura and Arie [21]. Figure 4-1 gives the definition of a linear shear flow. They concluded that in a linear shear flow R_{crit} was higher than in a uniform stream, that vortex shedding can disappear for R_e as high as 200 if shear is large enough and that R_{crit} increased approximately linearly with the increase in the shear parameter K in the range $K \geq 0.06$. Therefore, considering a dowel array, we expect the shear flow

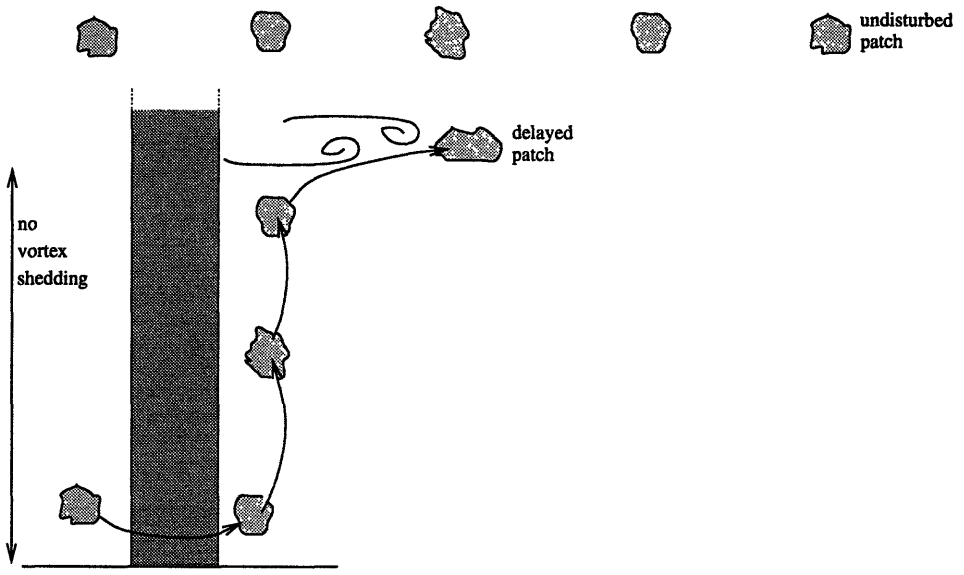

Figure 4-2: Delaying Process of Dye Trapped in the Backflow Region

created by the wake of dowels to interact with downstream dowels and to substantially affect their vortex shedding.

Zavistoski also demonstrated the existence of an upward pressure-driven current on the downstream side of the dowel, and of a similar downward pressure-driven current on the upstream side of the dowel. She also pointed out that at the toe of the dowels, due to the shear of the bed, R_e is below R_{crit} which prevents vortex shedding. Vortex shedding occurs only above one third of the flow depth. If we define "dead-zones" as regions which communicate with the free stream only by diffusion, Zavistoski's results show that the vortex-free backflow region behind the lower part of the dowels is not a real "dead-zone". As a matter of fact the upward current drives the dye from the lower part to the upper part of the dowel where dye is then spread into the flow because of vortex shedding. Nevertheless the region immediately behind the dowel can create a substantial delay for the dye patches that get caught in the ascendant current as shown on figure 4-2. Intuitively we can think that this delay is all the more important as the vortex shedding region is small, i.e. as R_e is small.

Therefore R_e is a critical parameter. It enhances the free stream turbulence with vortex shedding and affects the characteristics of the backflow region.

u_{inf}	C_1	C_d	$b(x)$	β
3 $cm.s^{-1}$	0.38	1.5	$0.79\sqrt{x}$	0.0416
12 $cm.s^{-1}$	0.5	1.1	$0.52\sqrt{x}$	0.0285

Table 4.1: Wake Characteristics

4.3 Shear Flow in the Wake of a Dowel

Wake theory can be used to describe the flow pattern downstream of the dowel. From Schlichting [18],

$$\frac{u_1}{u_{\text{inf}}} = \frac{u_{\text{inf}} - u}{u_{\text{inf}}} = \frac{\sqrt{10}}{18\beta}\left(\frac{x}{C_d d}\right)^{-\frac{1}{2}}\left[1 - \left(\frac{y}{b}\right)^{\frac{3}{2}}\right]^2,$$

with

$$C_1 = \frac{\sqrt{10 C_d d}}{18\beta},$$

and

$$b = \sqrt{10}\beta(x C_d d)^{\frac{1}{2}},$$

where u_{inf} is the free stream velocity, u the velocity inside the wake, u_1 the velocity loss inside the wake, C_d the coefficient of drag, d the dowel diameter, b the width of the wake, β the proportionality constant between the mixing length and b, and x the distance behind the dowel.

$b(x)$ can be obtained from the values of C_1 and C_d given by Zavistoski (table 4.1).

Knowing $b(x)$ is important for assessing dispersion effects due to shear flow in the wake of the dowel.

If we consider a dye cloud passing an individual dowel, the non-uniformity in the longitudinal velocities in the wake affects the shape of the cloud. The change in the shape persists when the cloud has left the wake. However, if diffusive effects are neglected, the shape of a dye cloud going through an array of randomly spaced dowels will on average remain undistorted as the stretching due to each individual dowel wake may be cancelled by the effect of another dowel downstream. If diffusive effects are also considered, lateral spreading between consecutive dowel wakes can

contribute to a net longitudinal dispersion.

Therefore two spreading effects can occur in the wake of the dowel. Longitudinal stretching occurs because of differential advection; this distortion cancels on the average. Lateral spreading may occur to smooth lateral concentration gradients across a wake introduced by the longitudinal stretching; by making an intuitive analogy with Taylor's dispersion theory, we expect the cloud to be globally stretched and longitudinal dispersion to be enhanced. The comparison of two time scales can help us assess the relative magnitude of those two spreading effects.

Figure 4-3 on page 34 is a schematic of the distortion process between consecutive dowels. The time for the dye patch to travel between consecutive dowels is $t_{adv} = S/\bar{u}$ where S is the average longitudinal length between two consecutive dowels.
A net longitudinal dispersion effect will be experienced on the average as soon as some "substantial" lateral mixing appears across the wakes. The lateral mixing need not be complete. A lateral mixing length λ is defined as the length scale across which lateral mixing must occur to observe a net longitudinal dispersion. As the dispersion process in the wake of the dowels is a dowel scale process, λ should scale on the diameter d of the dowels. We assumed $\lambda = 3d$. Therefore, the time for substantial lateral spreading to occur across the wake is $t_{diff} = \lambda^2/4D_w$ where D_w is the lateral diffusion coefficient in the wake of the dowel. The relative importance of lateral diffusion effects in the wake can be assessed by the dimensionless coefficient

$$t^+ = \frac{t_{adv}}{t_{diff}} = \frac{4SD_w}{\bar{u}\lambda^2} = \frac{4}{9}\frac{SD_w}{\bar{u}d^2}.$$

If this coefficient is much less than one, then only longitudinal stretching is observed because diffusive effects have no time to appear. On the contrary if this coefficient is much larger than one, we expect lateral spreading effects of dye within the wake of the dowel to be important, and longitudinal dispersion will be enhanced. This dimensionless coefficient parameterizes the presence of shear flow dispersion in the wake of the dowels. It will be estimated in section 5.3.3 to help us determine when shear flow dispersion in the wake of each dowel contributes to the "global" dispersion

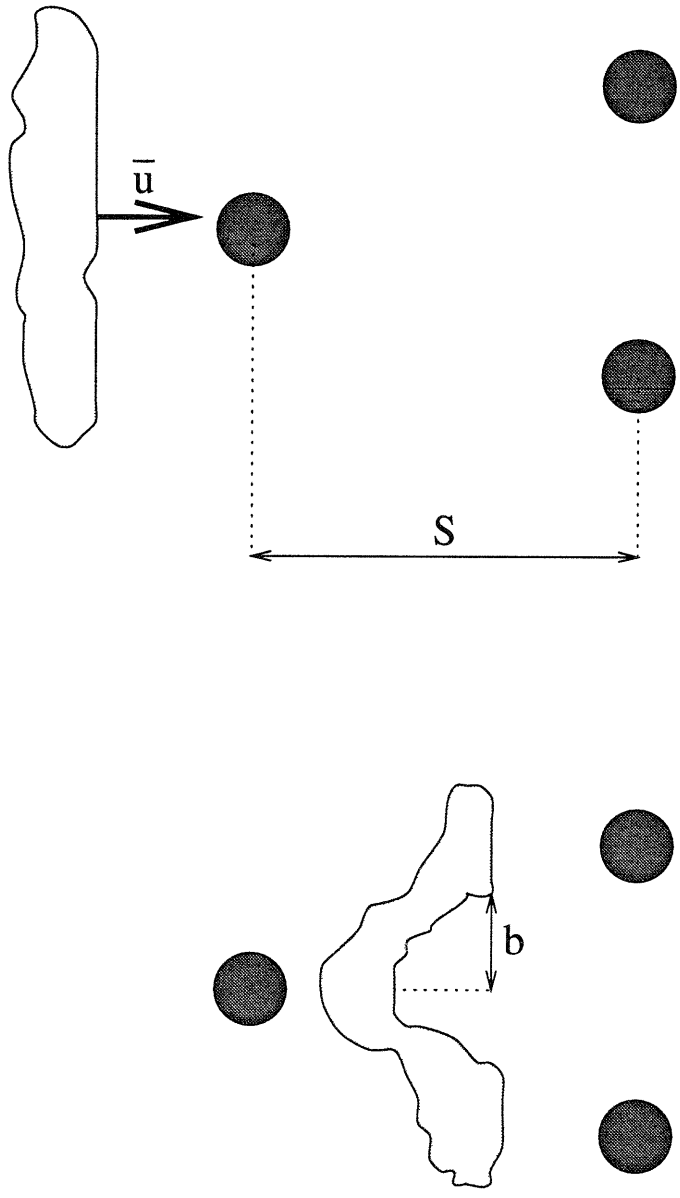

Figure 4-3: Distortion of a Dye Cloud Between Consecutive Dowels

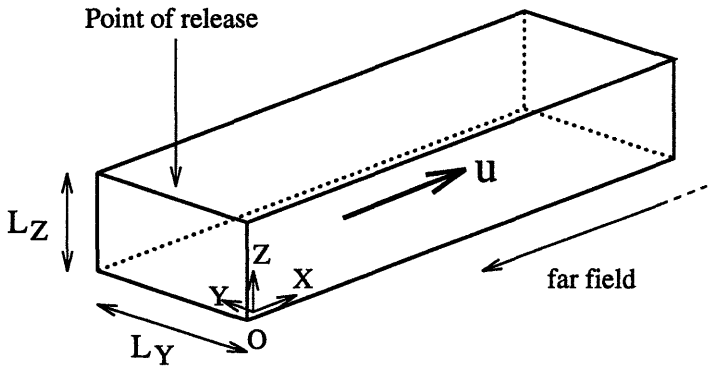

process.

4.4 Mathematics

The equation describing the one-dimensional diffusion process of any contaminant dumped in a flow is

$$\frac{\partial C}{\partial t} + u\frac{\partial C}{\partial x} = D_x \frac{\partial^2 C}{\partial x^2}, \tag{4.1}$$

where C and u are, respectively, the concentration of contaminant and the flow velocity in the longitudinal direction, and D_x is the longitudinal diffusion coefficient. In real flows, 3-D effects such as the non-uniformity of the longitudinal velocity across a cross-section of the channel create dispersion. As already stated in the previous chapters, Taylor studied shear flow dispersion and gave a model analogous to the one-dimensional diffusion process (equation 2.1 on page 12). Therefore, the mathematical solutions of the one-dimensional diffusion process given in the following paragraphs can be adapted to get mathematical solutions of the one one-dimensional dispersion process simply by replacing D_x by K. The analytical expression describing the concentration of contaminant downstream of an instantaneous point source release is

$$C(x,t) = \frac{M}{\sigma\sqrt{2\pi}} \exp\left[-\frac{(x-ut)^2}{2\sigma^2}\right], \tag{4.2}$$

where $\sigma = \sqrt{2D_x t}$ is the square root of the variance of the contaminant cloud and M is the total mass of contaminant dumped at $x = 0$. The analytical expression describing the front of a contaminant cloud downstream of a continuous release point is

$$C(x,t) = \frac{\dot{M}}{u} erfc\left(\frac{x-ut}{\sqrt{2}\sigma}\right), \tag{4.3}$$

where $\dot{M}$ is the constant rate of release of the contaminant at $x = 0$. At a fixed downstream location, as t goes to infinity C tends towards the constant $\dot{M}/u$. This is the steady-state value of the downstream concentration.

These mathematical solutions are valid only when the diffusion process is really one-dimensional, i.e., when the contaminant is fully mixed across a cross-section of the flow. This occurs at a downstream location

$$x \gg max\left[\frac{uL_y^2}{4D_y}, \frac{uL_z^2}{4D_z}\right]. \tag{4.4}$$

This spatial region is called the far field. In the case of dispersion, the condition is more stringent and corresponds to the time it takes for the dispersion process to become Fickian, so that the 1-D dispersion equation would only apply for

$$x \gg max\left[\frac{uL_y^2}{D_y}, \frac{uL_z^2}{D_z}\right]. \tag{4.5}$$

In the two particular cases presented above, the spatial variance of the cloud is given by $\sigma = \sqrt{2D_x t}$. The more general relationship between D_x and σ is

$$D_x = \frac{1}{2}\frac{d\sigma^2}{dt}, \tag{4.6}$$

which is true whatever the initial concentration distribution is, e.g., even if the distribution is spatially skewed. This relationship is true as long as the spreading of the contaminant cloud behaves according to a Fickian diffusion process.

If we know the spatial distribution of a point-released cloud, we can deduce σ knowing that 68% of the contaminant mass is within $[ut - \sigma, ut + \sigma]$.

If we know the concentration-time curve at a fixed point downstream of a continuous release, we can get D_x knowing that :

$$D_x = \frac{1}{2}\frac{{\sigma_{0.84}}^2 - {\sigma_{0.16}}^2}{t_{0.84} - t_{0.16}}, \tag{4.7}$$

where ${\sigma_{0.84}}^2$ and ${\sigma_{0.16}}^2$ are the variances of the cloud when C is, respectively, 16% and 84% of the steady-state concentration value.

4.5 Data Analysis

4.5.1 Estimate of K

From the experimental curves of concentration $C_0(t)$ of dye versus time at a fixed location downstream of the continuous release point, it is possible to get esimates of K. We already know that the theoretical concentration solution is an error function when Taylor's analysis applies. Assuming that our experimental curves are error functions, we can back-calculate K.

Rough estimate

A quick estimate of K can be obtained from :

$$K = \frac{1}{2}\frac{{\sigma_{0.84}}^2 - {\sigma_{0.16}}^2}{t_{0.84} - t_{0.16}}. \tag{4.8}$$

${\sigma_{0.84}}^2$ and ${\sigma_{0.16}}^2$ can be read from the experimental record. As this method is based only on two points of the curve and does not take into account its whole shape, it is imprecise. Nevertheless it gives a correct order of magnitude : $K = o(10)$.

Least-squared fit

This method consists of fitting the experimental curve with an error function. The theoretical concentration solution normalized based on the steady state concentra-

tion $(\dot{M}/u)$ is :

$$C_{th}(t) = \frac{1}{2} erfc \left(\frac{x - \bar{u}(t - \Delta t)}{\sqrt{4K(t - \Delta t)}} \right), \tag{4.9}$$

where x is the coordinate of the observation point (960 cm), $\bar{u}$ is the mean flow velocity in the flume, Δt the time lag due to the pumping system (3 s) and K the unknown dispersion coefficient. The mean flow velocity can theoretically be measured with the flowmeter but due to its low resolution, this method is not reliable. Therefore $\bar{u}$ is a second unknown. Estimates of $\bar{u}$ and K were found by minimizing the squared distance between the theoretical concentration solution C_{th} and the observed values C_0, i.e. minimizing

$$\varepsilon = \sqrt{\int_{-\infty}^{+\infty} [C_0(t) - C_{th}(t)]^2 dt}. \tag{4.10}$$

Several values of this distance were computed for an array of (K,$\bar{u}$). The array was created around a rough estimate of the solution (K',u') where K' is given by the first method and u' is read on the flowmeter.

4.5.2 Corrected Estimate

The problem with the previous method is that it implicitely considers that dispersion processes in both the no-dowel zone and the dowel zone are described by the same K. Therefore using it would not give the correct value of the dispersion coefficient in the dowel zone but an average of the dispersion coefficients of the two different zones.

In order to get an estimate of K which does not reflect the influence of the no-dowel zone, an analysis similar to Fischer's routing technique can be performed between the beginning and end of the dowel array (see figure 4-4).

Based on the concentration measurements performed for the no-dowel case, K_0 the dispersion coefficient of the no-dowel zone could be estimated by applying the basic method explained in section 4.5.1. Knowing K_0, K and u can be estimated by fitting the theoretical solution $C_{th\ 2}(t)$ at position 2 downstream of the dowel array (figure 4-4) to the experimental data $C_o(t)$. The theoretical profile at position 2

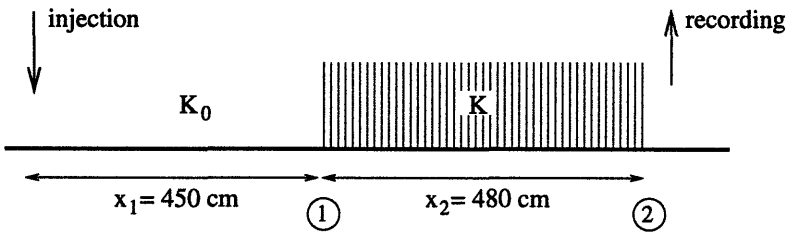

Figure 4-4: Description of the Corrected Estimate of K

is

$$C_{th\ 2}(t) = \int_0^t C_{th\ 1}(\tau) \frac{u}{\sqrt{4\pi(t-\tau)}} exp\left(-\frac{(x_2 - u(t-\tau))^2}{4K(t-\tau)}\right) d\tau, \tag{4.11}$$

where $C_{th\ 1}(t)$ is the theoretical solution upstream of the dowel array at position 1 :

$$C_{th\ 1}(t) = \frac{1}{2} erfc\left(\frac{(x_1 - ut)}{\sqrt{4K_0 t}}\right). \tag{4.12}$$

In the previous equations, x_1 is the distance from the release point to the dowel array and x_2 is the length of the dowel array as shown on figure 4-4.

An implicit assumption of this method is that while passing through x_1 the cloud does not have time to disperse. The Peclet number

$$P_e = \frac{x_1 u}{K}$$

being of the order of 100, the assumption is correct.

When matching theoretical and experimental curves, the time lag Δt due to the pumping system was again taken into account by changing t to $(t - \Delta t)$ in equation 4.11.

All numerical calculations were performed on MATLAB.

Chapter 5

Results and Discussion

All the experimental curves were normalized based on the average steady state value of the concentration. Usually, the experiments were performed twice for each set of parameters density-velocity and only the smoother curve of the two was considered for the least-squared fit computation. It is the curve given in the appendices.

5.1 Estimates of K from the Experimental Curves

The Reynolds numbers evaluated below are based on the diameter of the dowels (0.6 cm) :

$$R_e(d) = \frac{ud}{\nu}.$$

5.1.1 No-Dowel Cases

The experimental curves corresponding to the no-dowel cases are given in appendix A on page 65.

In the medium and the high velocity cases, the shape of the concentration curves was artificially smoothed by a 50 cm long very dense dowel array placed upstream of the recording point. Its dramatic effect on the curves can be seen by comparing figures A-1 and A-2. The fact that dye sampled at the recording point is not naturally well-mixed can be theoretically verified considering the length scale for complete

	velocity		
	low	medium	high
u $(cm.s^{-1})$	2.9	5.5	7.4
K $(cm^2.s^{-1})$	6	7	7

Table 5.1: Estimates of K_0 ; No-dowel Cases

mixing in the vertical which was found to be 11 m at medium velocity (section 3.2 on page 24), which is more than the distance from the release point to the recording point (960 cm).

The limited length of the flume is a more stringent problem when considering the length scale of the dispersion process. From Fischer the dispersion process becomes Fickian only at a distance $\bar{u}h^2/D_{t\ z}$ from the release point (equation 4.5). An estimate of this distance based on $D_{t\ z} = 0.5\ cm^2.s^{-1}$ (section 3.2) is 48 m. The condition on the use of the routing procedure is less limiting but leads to a minimum distance of 19 m ($0.4\ \bar{u}h^2/D_{t\ z}$) which is again more than the experimental distance available.

Therefore we can expect our experimental results to underestimate the dispersion process which does not have time to fully appear due to the limited length of the flume and since the process is abruptly stopped before being fully developed by the short distance of dowels added just upstream of the recording location. This can be checked out by comparing our results with Elder's formula (2.4) which gives $K \approx 100\ cm^2.s^{-1}$, i.e., one order of magnitude higher than our measures.

Finally, it is worth noting that the estimated K does not depend on the flow velocity.

5.1.2 Dowel Cases

The experimental curves corresponding to the dowel cases are given in appendix B on page 68.

The theoretical solution corresponding to a continuous release is an error function, as already stated in section 4.4 on page 35. If the dispersion process in the flume was

purely Fickian, the experimental curves would be error functions. It appeared that trying to fit an error function with the whole experimental curve would systematically incorrectly match the initial rise of the curve and its approach to steady-state. But trying to fit an error function with only the first half of the experimental curve would lead to more satisfactory results. From these observations, it can be suspected that only the initial rise of the curve corresponds to a purely Fickian dispersion process. The estimates of K were obtained from the corrected estimate method explained in section 4.5.2 applied to the first half of the curves. Figure 5-1 pictures this partial fit for the low velocity - low density case, and figure 5-2 illustrates the lag between the second halves of the corresponding error function and experimental curve.

Since the area below the curves corresponds to the quantity of advected dye and since the experimental curve is systematically lower than the estimated error function curve, the mismatch between the second halves of those curves can be attributed to a delay phenomenon. Section 5.3.1 numerically models the idea that a backflow region can act as a delaying zone and confirms that this phenomenon can substantially affect the "global" dispersion process.

The estimates of K are listed in tables 5.2, 5.3 and 5.4. They are based on the estimates of K_0 given in table 5.1. According to the accuracy of the estimation method, it appears that neither the flow velocity nor the dowel density seem to significantly affect the value of K. In all the cases K is lower than 5 $cm^2.s^{-1}$. Therefore, at each velocity K is lower than the corresponding K_0. The only hydrodynamic process that could lead to a decrease of K is the decrease of shear flow dispersion due to the bed. This can occur either by an increase in the vertical turbulent diffusion or by the downward extension of the uniform velocity layer in the dowel array compared to the no-dowel case. An estimate of the order of magnitude of shear flow dispersion due to the bed is presented in section 5.3.4.

Features of the Delay Process From the experimental curves, two main features can be drawn. First, in most of the cases, between 10% and 30% of the mass will experience the delay process. This can be seen from the fact that the percentage of

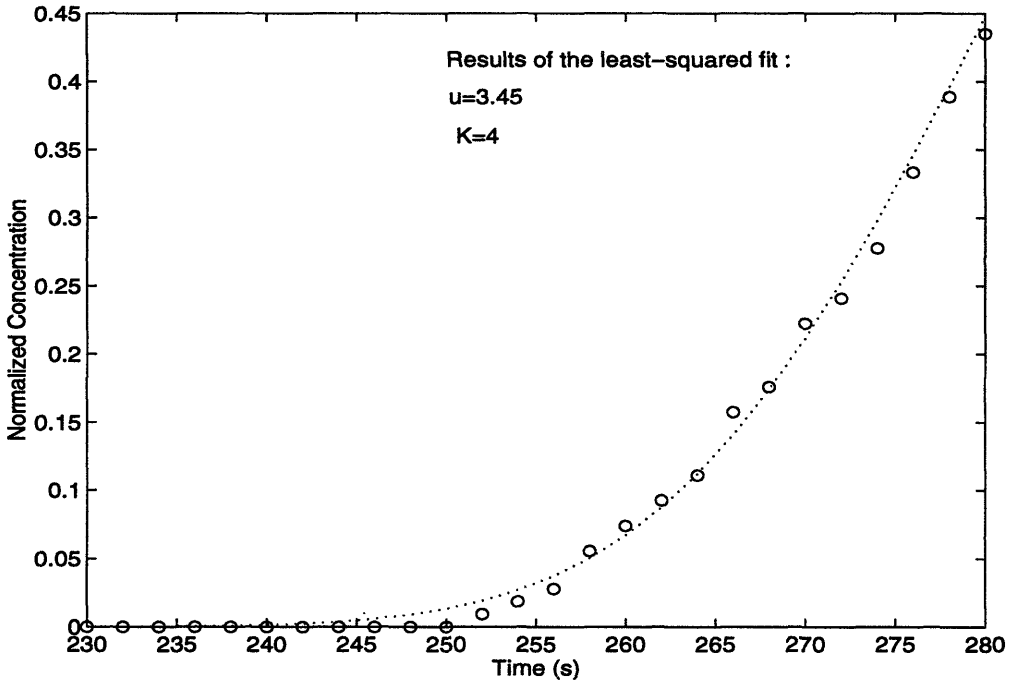

Figure 5-1: Example of Incomplete Fit (medium density, low velocity)

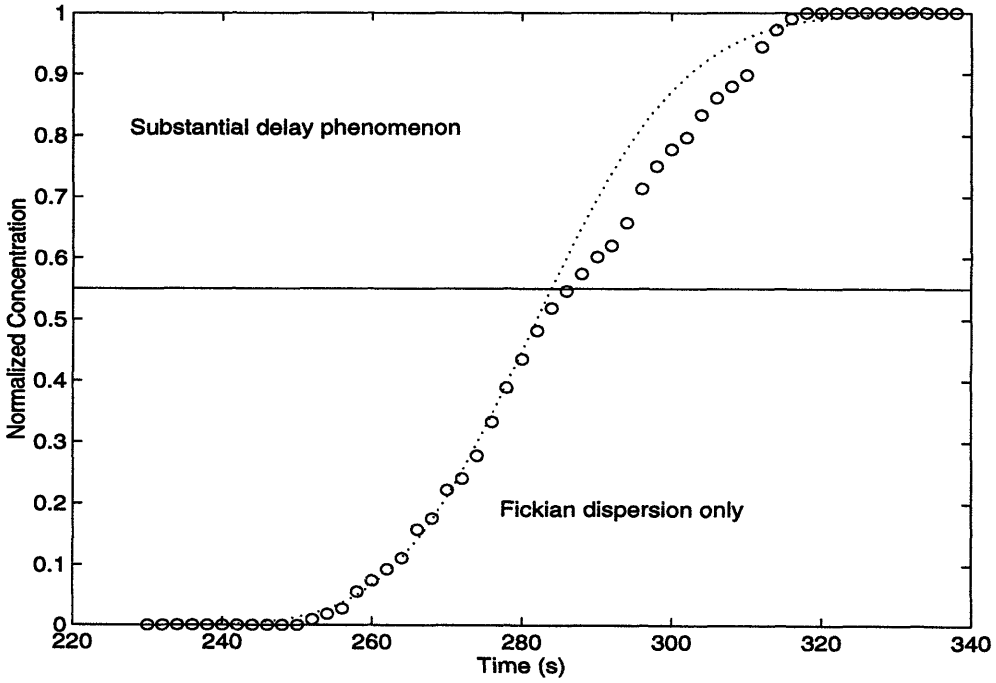

Figure 5-2: Observation of the delay Phenomenon (medium density, low velocity)

	velocity		
	low	medium	high
$u\ (cm.s^{-1})$	3.45	5.55	7.45
$K\ (cm^2.s^{-1})$	4	3	4
$R_e(d)$	210	330	450

Table 5.2: Estimates of K ; low density

	velocity		
	low	medium	high
$u\ (cm.s^{-1})$	2.95	5.05	7.45
$K\ (cm^2.s^{-1})$	1	3	5
$R_e(d)$	180	300	450

Table 5.3: Estimates of K ; medium density

	velocity		
	low	medium	high
$u\ (cm.s^{-1})$	2.83	5.28	7.55
$K\ (cm^2.s^{-1})$	4	1	4
$R_e(d)$	170	320	450

Table 5.4: Estimates of K ; high density

mass that does not experience the delay is simply given by the value of normalized concentration above which experimental and theoretical curves no longer match. The maximum value of this percentage is 50% and corresponds to the low density, low and medium velocity cases. According to the accuracy of the estimations, no particular relation or trend could be determined between the percentage of dye experiencing the delay and either the flow velocity or the dowel density. Second, the length of the tail can be estimated from the time during which experimental and theoretical curves do not match, knowing the flow velocity. In all the cases the tail length was estimated between 100 *cm* and 150 *cm* which is significant compared to the length of the dowel array (480 *cm*).

5.2 Error-Analysis

The purpose of this section is to assess the accuracy of the estimates of K presented in the previous section.

5.2.1 Dispersion in the Pumping System

The fluorometer was used in a continuous flow mode, and water was pumped from the flume through a half centimeter diameter flexible plastic tube : the pumping rate q was constant and could vary between 2 and 20 $cm^3.s^{-1}$. Flow rates close to 20 $cm^3.s^{-1}$ were not used as vibrations would propagate along the tube and disturb the flow. The length of the tube L was approximately 1.5 m.

The point of the following analysis is to determine if dispersion within the tube can substantially bias our estimations of dispersion coefficients.

The following analysis is based upon $q = 8\ cm^3.s^{-1}$, $L = 1.75\ m$ and $a = 0.25\ cm$ where a is the radius of the plastic tube. Therefore

$$R_e = \frac{2q}{\pi a \nu} = 2040$$

This value is close to the threshold value 2300. Therefore the analysis was performed considering both the laminar and the smoothly turbulent cases.

Laminar case Taylor's analysis describes shear flow dispersion in a cylindrical tube assuming laminar conditions and a parabolic cross sectional velocity profile :

$$u(r) = u_0 \left(1 - \frac{r^2}{a^2}\right),$$

where r is the distance from the central axis of the tube, and u_0 twice the mean velocity through a cross section. $u_0 = 80\ cm.s^{-1}$. Taylor gives

$$K = \frac{a^2 {u_0}^2}{192D},$$

where D is the molecular diffusivity of the traced substance. Taylor's analysis is valid only after an initial period of time :

$$t_i = \frac{a^2}{3.8^2 D}.$$

$D_{rhodamine}$ was found to be approximately $5\times10^{-6}\ cm^2.s^{-1}$. This value gives $t_i = 865\ s$. The advective time being of the order of $L/\bar{u} = 3\ s$, shear flow dispersion does not have time to appear.

Let C_i and C_o be respectively the concentration of Rhodamine entering the tube from the flume and the concentration entering the fluorometer. If advection is the only source of dispersion, it can be found from Taylor [22] that :

$$C_o(t) = \int_{-\infty}^{t-\frac{x}{u_0}} \frac{\partial C_i}{\partial t}(\tau)\left[1 - \frac{x}{u_0(t-\tau)}\right] d\tau, \tag{5.1}$$

which simplifies to

$$C_o(t) = \int_{-\infty}^{t-\frac{x}{u_0}} C_i(\tau)\left[\frac{x}{u_0(t-\tau)^2}\right] d\tau \tag{5.2}$$

when $C_i(t=-\infty) = 0$. During the experiments, we worked with the measures of C_o given by the fluorometer. In order to check whether or not estimates based upon C_o are reliable, C_o was numerically computed from 5.2 with C_i equal to the theoretical solution for a continuous release, i.e.

$$C_i(x,t) = \frac{1}{2}\ erfc\left(\frac{x-\bar{u}t}{\sqrt{2}\sigma}\right), \tag{5.3}$$

where $\sigma = \sqrt{2Kt}$. We chose $x = 500\ cm$ and $u = 3\ cm.s^{-1}$. Two cases were studied, C_i described by :

- K=5 $cm^2.s^{-1}$.
- K=75 $cm^2.s^{-1}$.

Estimates of K were then obtained by a least-squared fit of an error function with the C_0 curve and compared to the input values given above. Δt designates the time

lag due to advection through the tube between C_0 and C_i.

K	$\Delta t(s)$	*Estimated u*	*Estimated K*	% Error
5	8	3	7	40
75	9	2.85	78	4

Turbulent case In this case we assumed that the mixing of dye is similar to the mixing of momentum, i.e., that D_t and ν_t are equal. Taking $u^* = \sqrt{f/8}\bar{u}$ and $f = 0.04$ for a smooth pipe, and from

$$\nu_t = \kappa u^* a \left(1 - \frac{r}{a} - \left(1 - \frac{r}{a}\right)^2\right)$$

in a pipe, we could estimate

$$D_t \approx \ 0.2u^* a \approx 0.14 \ cm^2.s^{-1}.$$

This led to $t_i \approx 0.05 \ s$ which is much lower than the advective time. Therefore the shear dispersion in the tube is negligible if the flow is turbulent because cross-sectional mixing is so rapid.

$$C_0(t) = \int_{-\infty}^{t} \frac{C_i(\tau)u_0}{\sqrt{4\pi K_{tube}(t-\tau)}} exp\left[-\frac{(x - u_0(t-\tau))^2}{4K_{tube}(t-\tau)}\right] d\tau \tag{5.4}$$

From Taylor $K = 10.1au^*$ and we found $K = 7 \ cm.s^{-1}$. We performed a similar analysis to that of the laminar case.

K	$\Delta t(s)$	*Estimated u*	*Estimated K*	% Error
5	4	3	5	0
75	4	2.85	69	8

Under such conditions $P_e = o(1000)$ and it is logical to find $\Delta t = t_{adv} = 4 \ s$.

Conclusion Therefore, the best way to minimize the error due to dispersion inside the tube is to create turbulence in the tube. In our experiments we used $q = 13\ cm^3.s^{-1}$. Even if R_e was still close to the threshold value the pumping system would trip the flow and make it fully turbulent. This would lead to $\Delta t = t_{adv} = 3\ s$. Under these conditions we can assume that the pumping system does not affect the dynamic concentration measurements.

5.2.2 Error in the Estimate of K

The corrected method explained in section 4.5.1 was used to estimate K and u for each experiment. Only discrete values of K and u were considered. The precision on K and u was respectively 1 $cm^2.s^{-1}$ and 0.05 $cm.s^{-1}$.

An analysis of the values of the least-squared fit error ε given by equation 4.10 shows that, contrary to u, the optimum value of K was not always well definite as the error did not significantly vary with K. The estimating of K for the no-dowel high velocity case illustrates this problem. Once the optimum velocity was set to 7.4 $cm.s^{-1}$, three values of K would lead to values of ε within a range of 10% of the minimum error.

$K(cm^2.s^{-1})$	5	6	7	8	9	10	11
ε^2	.0370	.0254	**.0206**	**.0208**	**.0245**	.0309	.0393

A look at figure 5-3 shows that the three corresponding curves are hardly distinguishable. Beside, the uncertainty in the estimate of K_0 would add uncertainty to the estimates of K in the dowel cases. For this reason, only the order of magnitude of K could be estimated. Values of K between 1 and 5 cannot be considered as significantly different.

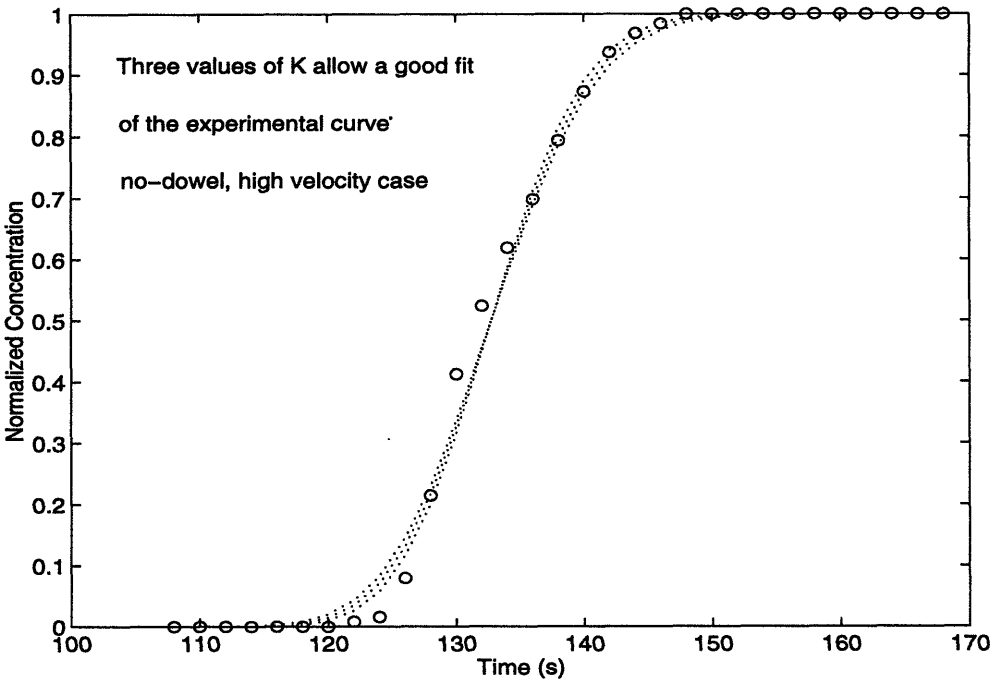

Figure 5-3: Illustration of the Uncertainty in the Estimates of K

5.3 Assessement of the Dispersive Effects Governing Longitudinal Dispersion

The purpose of this section is to give the order of magnitude of each of the dispersion processes likely to appear in the experiments.

5.3.1 Estimate of Dispersion due to Delay Zones

We already know that the backflow zone behind each dowel delays trapped fluid particles. The purpose of this section is to assess whether or not the delay can significantly affect the global dispersion coefficient and explain the substantial delay phenomenon already observed when analyzing the experimental curves.

A simple numerical study of a slug release through an array of dowels was done, neglecting every source of dispersion but the delay phenomenon.

Description of the Model

In section 4.2 on page 31 we already stated that the vortex-free backflow region behind a dowel does not exactly follow Valentine's definition of "dead-zone". Valentine's dead-zones are no-flow regions which communicate with the free-stream only by turbulent diffusion which is not true in our case since an upward current exists in a backflow region. Therefore, the backflow region we are interested in was given the name delay-zone as opposed to dead-zone.

Figure 4-2 on page 31 already described the process delaying a patch of dye trapped in the backflow region. An intuitive approach of the problem consisted in modeling a delay zone as a linear queue of trapped dye patches. We also assumed no mixing in the dead-zones so that trapped dye patches were only delayed. After being kept for a time ΔT in a dead-zone dye patches are released back to the free stream were they mix instantly with the advecting dye, i.e., we assume instant cross sectional mixing out of the delay-zones.

Let Δx and Δt be the spatial and temporal steps of the model. The model computes the values of $C_{(I,J)}$ the free-stream concentration at each point (I, J) of the corresponding space-time grid system according to the following process. For each time J, at each spatial point I, a portion A of the free-stream dye is being trapped in the corresponding local dead-zone. Simultaneously the dye that had been trapped ΔT before is being released and instantly mixed in the free-stream. At this stage of the process, advection is taken into account by spatially translating the values of the free-stream concentration. Outside the dowel zone only advection is taken into account and the delaying process is skipped.

Equations of the Model

The mathematical translation of the process described above is :

Outside the dowel array,

$$C_{(I,J+1)} = \underbrace{C_{(I-N,J)}}_{\text{advected concentration}} . \tag{5.5}$$

Inside the dowel array,

$$C_{(I,J+1)} = \underbrace{C_{(I-N,J)}}_{\text{advected concentration}} - \underbrace{A.C_{(I,J)}}_{\text{trapped concentration}} + \underbrace{A.C_{(I,J-M)}}_{\text{released concentration}} , \tag{5.6}$$

where

$$N = u.\frac{\Delta t}{\Delta x} \tag{5.7}$$

corresponds to the advection translation,

$$M = \frac{h}{3}\frac{1}{\Delta t\ w} \tag{5.8}$$

corresponds to the delay inside a dead-zone[1], and

$$A = \frac{\mathcal{D} w \Delta t}{h} \tag{5.9}$$

is the fraction of free-stream flow trapped inside dead-zones at each time step.

Parameters The parameters of the model were the upward flow velocity w inside the delay-zones, the volume of the delay-zone, the free stream velocity u, the diameter of a dowel d (0.6 cm) and the dowel density $\mathcal{D}$.

From Zavistoski, w was estimated to be approximately 20% of u. Backflow regions behind a cylinder typically extend one diameter downstream. Flow visualization showed that the height of the backflow region is approximately one third of the total flow depth.

The dowel array we considered was 450 cm long and started 150 cm downstream of the release point. Δx and Δt are set, the two parameters governing the model are u and $\mathcal{D}$, the overall constraint being that N and M given by equations 5.7 and 5.8 have to be integers. In a first set of experiments, u was set to 6 $cm.s^{-1}$ and three densities were studied, a medium density (1%), a high density (5%) and a very high density (25%). In a second set of experiments, the density was set to 5% and two

[1]If the heigth of the no vortex shedding region is $h/3$ as stated below.

flow velocitiess were studied, a very low velocity (0.6 $cm.s^{-1}$) and a medium velocity (6 $cm.s^{-1}$).

Results of the Model and Discussion

We considered a slug release which led to an additional set of equations :

$$\begin{cases} C_{(1,0)} = 1 \\ \forall I > 0,\ C_{(I,0)} = 0 \end{cases}$$

For both densities the center of mass, m, and the spatial variance, σ^2 of the cloud were computed and plotted versus time.

$$\begin{cases} m_{(J)} = \sum_I C_{(I,J)} I\Delta x \\ \sigma^2{}_{(J)} = \sum_I C_{(I,J)} (I\Delta x)^2 - {m_{(J)}}^2 \end{cases}$$

The vertical lines represent the time the cloud enters and leaves the array of dowels.

The cloud velocity and the dispersion coefficient K could be estimated from the slopes of the curves. It can be seen that the variance grows linearly with time. This result was not obvious because the governing process is not a diffusion phenomenon but a delay phenomenon ; it creates a tail such that the spatial concentration curve is not apparently gaussian. This relates to the theoretical study by Chikwendu and Ojiakor [2]. They showed that a tail can be considered as a a large gaussian followed by a small gaussian. Therefore they proved that a delay can be gaussian and still cause a tail. Figure 5-4 and Figure 5-5 show that K increases with both the density and the velocity. At $u = 6\ cm.s^{-1}$, K was estimated to be 1.87 $cm^2.s^{-1}$ for the high density and 7.33 $cm^2.s^{-1}$ for the very high density. Those values are the same order of magnitude as the experimental estimations. We can therefore assume that the delay phenomenon contributes to the experimentaly observed net dispersion coefficient.

Because the cloud velocity was approximately equal to u no global delay is predicted by the model.

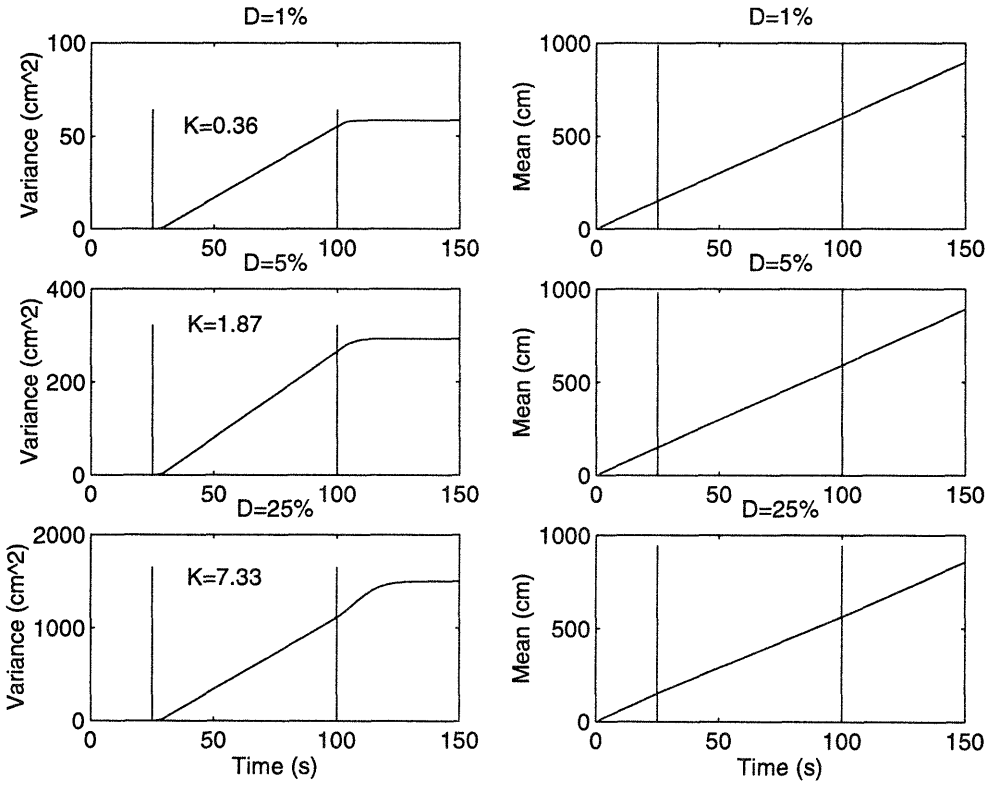

Figure 5-4: Results of the Numerical Model - *velocity* $= 6\ cm.s^{-1}$ - *various densities*

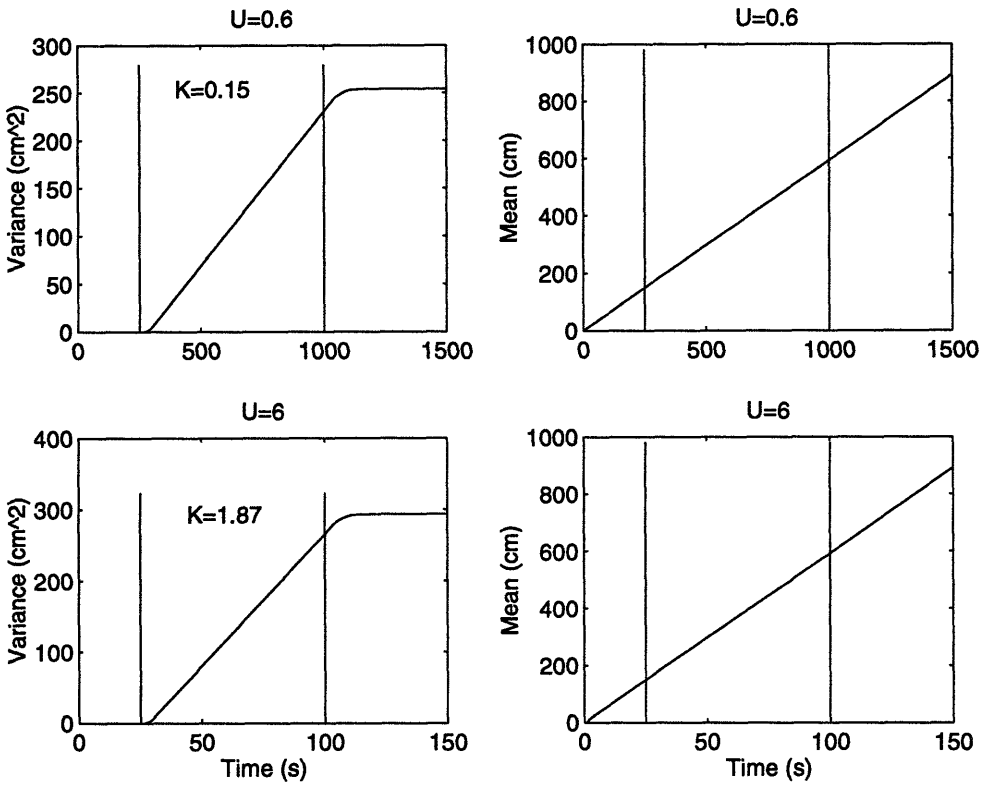

Figure 5-5: Results of the Numerical Model - *various velocities* - *density* = 5%

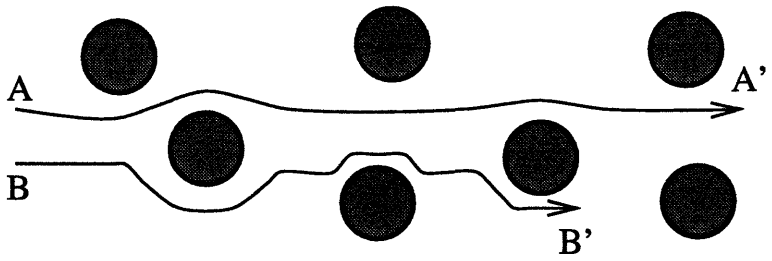

Figure 5-6: Schematic of Mechanical Dispersion

5.3.2 Estimate of Mechanical Dispersion

The spreading process due to dense obstructions within a flow is called mechanical dispersion. This simply means that fluid elements starting at a given distance from each other and proceeding at the same velocity will not remain the same distance apart, as shown on figure 5-6.

The purpose of this section is to give an estimate of the mechanical dispersion coefficient D_{mech}. Our analysis is based on a simple description of the mechanical process. Let x be the length of the dowel array we are interested in, $\mathcal{D}$ its density [2], and $\bar{u}$ the flow mean velocity. Let the dowel diameter d be the length scale of the process and let's decompose the total length x in one diameter long slices. A fluid particle starting at the entrance of the array can be delayed through each slice with a probability $\mathcal{D}$. Let dl be the average longitudinal distance lost each time a particle is delayed by a dowel. The total number of slices is $N = x/d$. In our experiments the dowel array is 500 cm long which gives $N \approx 1000$. The probability $P(n)$ for a particle leaving the array to have experienced n delays is simply given by a binomial distribution :

$$P(n) = C_N^n \mathcal{D}^n (1-\mathcal{D})^{N-n}.$$

When N is large enough[3] , the binomial distribution tends toward a normal distribu-

[2] $\mathcal{D}$ is the relative area of the dowel base ; it is a percentage.

[3] The typical criteria is $N\mathcal{D} > 5$. Therefore, our assumption is valid for densities as low as 1%.

tion the mean of which is

$$m = N\mathcal{D}$$

and the variance of which is

$$\sigma^2 = N\mathcal{D}(1 - \mathcal{D}).$$

Therefore, the spatial variance of the process is

$$\sigma^2 = N\mathcal{D}(1 - \mathcal{D})dl^2.$$

From the normality of the distribution, we can estimate D_{mech} :

$$D_{mech} = \frac{\sigma^2}{2t} = \frac{\sigma^2 \bar{u}}{2x} = \frac{\bar{u} dl^2}{2d} \mathcal{D}(1 - \mathcal{D}).$$

When $\mathcal{D}$ is low enough the previous result simplifies to :

$$D_{mech} = \left(\frac{dl^2}{2d} \right) \bar{u}\mathcal{D}.$$

Therefore D_{mech} does not depend on the length of the array. It is proportional to the flow velocity and to the dowel density, the proportionality constant $dl^2/2d$ being a function of the flow pattern around a dowel of diameter d. We can assume that dl is on the order of d. Taking $\bar{u} = 6\ cm.s^{-1}$, $\mathcal{D} = 5\ \%$ and $d = 0.6\ cm$ leads to $D_{mech} \approx 0.1\ cm^2.s^{-1}$. This value is one order of magnitude lower than the experimental estimated values.

We can conclude that mechanical dispersion does not contribute significantly to the experimentally observed dispersion process.

5.3.3 Estimate of Shear Flow Dispersion in the Wake of a Dowel

We already stated in section 4.3 that the relative importance of shear flow dispersion in the wake of a dowel can be assessed by the coefficient

$$t^+ = \frac{4}{9}\frac{S}{d^2}\frac{D_w}{\bar{u}}.$$

The purpose of this section is to estimate this coefficient for the selected velocities and densities.

Estimate of D_w

In order to estimate t^+, we need to know the cross-sectional diffusion coefficient in the wake D_w. Having no experimental value available, we had to estimate this coefficient. The idea of the estimation is that under turbulent conditions the mixing of dye is similar to the mixing of momentum. Therefore b^2 plays the role of the spatial variance σ^2 and D_w can be estimated from :

$$D_w = \frac{1}{2}\frac{b^2\bar{u}}{x}, \tag{5.10}$$

where $\bar{u}$ is the free flow velocity and b the wake half-width of the wake at a distance x downstream the dowel.

Because b being proportional to $\sqrt{x}$, D_w given by equation 5.10 will be independant of x. In order to estimate b we can use the results from Zavistoski and consider that β is a constant in the velocity range we consider. With a 15% accuracy we can assume $\beta = 0.35$, which leads to $D_w = 0.37 C_d \bar{u}$ with a 30% accuracy. Table 5.5 on page 59 gives the estimated values of D_w for different flow velocities.

Time scale of shear flow dispersion in the wake of a dowel

Knowing D_w, t^+ can be estimated. The values of S were already given in table 3.1 (page 23). Table 5.3.3 (page 59) gives the estimated values of t^+.

$\bar{u}(cm.s^{-1})$	$D_w(cm^2.s^{-1})$	$D_w/\bar{u}(cm)$
3	1.7 (1.2 - 2.2)	0.57
6	3.0 (2.1 - 3.9)	0.50
9	4.1 (2.9 - 5.3)	0.46

Table 5.5: Estimates of D_w

		density		
		low	medium	high
velocity	low	5.6296	3.3778	1.6889
	medium	4.9383	2.9630	1.4815
	high	4.5432	2.7259	1.3630

Table 5.6: Estimates of t^+

According to this analysis, t^+ barely depends on the flow velocity. It essentially depends on the density of the dowel array. Shear flow dispersion has time to appear between consecutive rows of dowels at each of the selected densities.

Estimate of K_w

The order of magnitude of this shear flow dispersion coefficient can be determined from Elder (equation 2.4 on page 14) using the velocity profile given by Schlichting. If the velocity profile is averaged in the x-direction between $x = 0$ and $x = S$, we are left with a simple lateral velocity profile that can be plugged in Elder's integral expression. This leads to :

$$K_w = \frac{0.012\ \bar{b}^2 \bar{C_2}^2 \bar{u}^2}{D_w}$$

where

$$\bar{b} = \frac{2}{3}\sqrt{10}\beta(SC_d d)^{\frac{1}{2}}$$

is the average half width of the wake and

$$\bar{C_2} = \frac{\sqrt{10}}{18\beta} 2\left(\frac{S}{C_d d}\right)^{-\frac{1}{2}}$$

is the average value between $x = 0$ and $x = S$ of

$$C_2 = \frac{\sqrt{10}}{18\beta}\left(\frac{x}{C_d d}\right)^{-\frac{1}{2}}.$$

$\bar{b}^2 \bar{C_2}^2$ is independant of S and β and is on the order of 10^{-1} to 1. This would lead to K_w on the order of 10^{-2} to 10^{-1} $cm^2.s{-}1$, i.e., one or two orders of magnitude lower than the experimental estimates of K. We can assume that shear flow dispersion in the wake of the dowels has negligible effect on "global" longitudinal dispersion.

5.3.4 Estimate of Shear Flow Dispersion Due to the Bed

The influence of shear flow dispersion can simply be determined from Elder's equation (2.4) using the volume average vertical velocity profiles given by Zavistoski [25] for each of the three densities. Zavistoski set the flow velocity U to 6 $cm.s^{-1}$. Elder's equation was discretized using a half meter length step. The notation $\mathcal{I}$ designates the integral :

$$-\frac{1}{h}\int_0^h u' \int_0^z \int_0^z u' \, dz \, dz \, dz.$$

Therefore $K = \mathcal{I}/D_y$, where D_y is the vertical diffusion coefficient.
In the low density case, we found $\mathcal{I} = 7.2$ $cm^4.s^{-2}$.
In the medium density case, we found $\mathcal{I} = 12.5$ $cm^4.s^{-2}$.

The significant feature of the profiles we used is that the boundary layer is depressed when the dowel density increases, i.e., the region of significant mean shear is reduced. Therefore, contrary to what we found above, $\mathcal{I}$ was expected to be lower in the second case. This unexpected result may be due to the uncertainty in the measurements of the vertical profiles. In the high density case the vertical profile was almost a vertical line and the uncertainty on the values of u' was too high to reliably compute $\mathcal{I}$.

Therefore, our analysis only provides us with the order of magnitude of $\mathcal{I}$. We can assume $\mathcal{I} \approx 10$ $cm^4.s^{-2}$.

For our analysis to be complete, some information about D_y is required. D_y is

the characteristic of vertical turbulent diffusion among the dowels. It is expected to increase with the flow velocity and the plant density. Experiments are currently being conducted by Sullivan at Parsons Lab, MIT, to acurately determine D_y and its correlations with the flow velocity and the plant density.

In our case, a rough estimate of D_y was performed. A drop of blue dye was released at the surface of the flow and the time t till it mixes to the bed was measured. The vertical diffusion coefficient could be estimated from

$$D_y = \frac{h^2}{4t}.$$

This led to $D_y \approx 1.5\ cm^2.s^{-1}$ at medium velocity and medium density and to $D_y \approx 0.5\ cm^2.s^{-1}$ at medium velocity in the no-dowel case. The corresponding K would be on the order of $10\ cm^2.s^{-1}$.

According to this analysis shear flow dispersion due to the bed is expected to be one of the dominant effects of the "global" dispersion process.

z	u/U	$\bar{u}/U$	u'/U	$\int_0^z \int_0^z u'/U \; dz \; dz$
0	0	0.986	-0.9860	0
0.5	0.8	0.986	-0.1860	-0.2930
1	0.95	0.986	-0.0360	-0.5950
1.5	0.97	0.986	-0.0160	-0.9011
2	0.97	0.986	-0.0160	-1.2111
2.5	0.975	0.986	-0.0110	-1.5239
3	0.9875	0.986	0.0015	-1.8364
3.5	1.00	0.986	0.0140	-2.1453
4	1.00	0.986	0.0140	-2.4508
4.5	1.0125	0.986	0.0265	-2.7497
5	1.02	0.986	0.0340	-3.0400
5.5	1.0250	0.986	0.0390	-3.3207
6	1.0375	0.986	0.0515	-3.5884
6.5	1.0375	0.986	0.0515	-3.8434
7	1.0375	0.986	0.0515	-4.0854
7.5	1.0375	0.986	0.0515	-4.3146
8	1.0375	0.986	0.0515	-4.5309
8.5	1.03	0.986	0.0440	-4.7362
9	1.025	0.986	0.0390	-4.9318
9.5	1.025	0.986	0.0390	-5.1177
10	1.025	0.986	0.0390	-5.2938
10.5	1.0375	0.986	0.0515	-5.4570
11	1.04	0.986	0.0540	-5.6068
11.5	1.05	0.986	0.0640	-5.7406
12	1.0625	0.986	0.0765	-5.8553
12.5	1.0625	0.986	0.0765	-5.9508
13	1.0625	0.986	0.0765	-6.0272
13.5	1.0625	0.986	0.0765	-6.0846
14	1.0625	0.986	0.0765	-6.1228
14.5	1.0625	0.986	0.0765	-6.1419
15	1.0625	0.986	0.0765	-6.1419

$$\mathcal{I} = 7.2 \; cm^4.s^{-2}$$

Table 5.7: Numerical Computation of $\mathcal{I}$ - low density

z	u/U	$\bar{u}/U$	u'/U	$\int_0^z \int_0^z u'/U \; dz \; dz$
0	0	0.9937	-0.9937	0
0.5	0.975	0.9937	-0.0187	-0.2531
1	0.975	0.9937	-0.0187	-0.5109
1.5	0.9625	0.9937	-0.0312	-0.7765
2	0.95	0.9937	-0.0437	-1.0530
2.5	0.9625	0.9937	-0.0312	-1.3373
3	0.9750	0.9937	-0.0187	-1.6263
3.5	0.9975	0.9937	0.0038	-1.9143
4	1.0200	0.9937	0.0263	-2.1958
4.5	1.0225	0.9937	0.0288	-2.4701
5	1.0250	0.9937	0.0313	-2.7365
5.5	1.0225	0.9937	0.0288	-2.9958
6	1.0200	0.9937	0.0263	-3.2484
6.5	1.0300	0.9937	0.0363	-3.4920
7	1.0400	0.9937	0.0463	-3.7241
7.5	1.0400	0.9937	0.0463	-3.9445
8	1.0400	0.9937	0.0463	-4.1534
8.5	1.0450	0.9937	0.0513	-4.3495
9	1.0500	0.9937	0.0563	-4.5315
9.5	1.0500	0.9937	0.0563	-4.6994
10	1.0500	0.9937	0.0563	-4.8533
10.5	1.0550	0.9937	0.0613	-4.9918
11	1.0600	0.9937	0.0663	-5.1137
11.5	1.0600	0.9937	0.0663	-5.2191
12	1.0600	0.9937	0.0663	-5.3079
12.5	1.0750	0.9937	0.0813	-5.3764
13	1.0675	0.9937	0.0738	-5.4264
13.5	1.0750	0.9937	0.0813	-5.4562
14	1.0750	0.9937	0.0813	-5.4656
14.5	1.0250	0.9937	0.0313	-5.4671
15	1.0	0.9937	0.0063	-5.4671

$$\mathcal{I} = 12.5 \; cm^4.s^{-2}$$

Table 5.8: Numerical Computation of $\mathcal{I}$ - medium density

5.4 Conclusion

The order of magnitude of dispersive processes likely to account for longitudinal dispersion in our experiments was systematically determined. Only shear flow dispersion due to the bed and the trapping in delay zones are expected to contribute significantly to the "global" dispersion process. The delay phenomenon was observed on the experimental concentration curves from which we found that less than 50% of the dye, usually between 20 and 30%, corresponded to a tail which was more than a meter long.

Considering the accuracy of our estimates, no dramatic effect on the longitudinal dispersion coefficient K was detected for either flow velocity or dowel density. Estimates of K with dowels ranged from 1 to 5 $cm^2.s^{-1}$. This represents a slight decrease of K in the dowel cases compared to the no-dowel cases where K ranged from 6 to 7 $cm^2.s^{-1}$. This difference could be explained by reduced shear-dispersion arising from a thinner boundary layer or enhanced vertical turbulent diffusion observed when the dowels were present.

Appendix A

Concentration Curves

No-dowel Cases

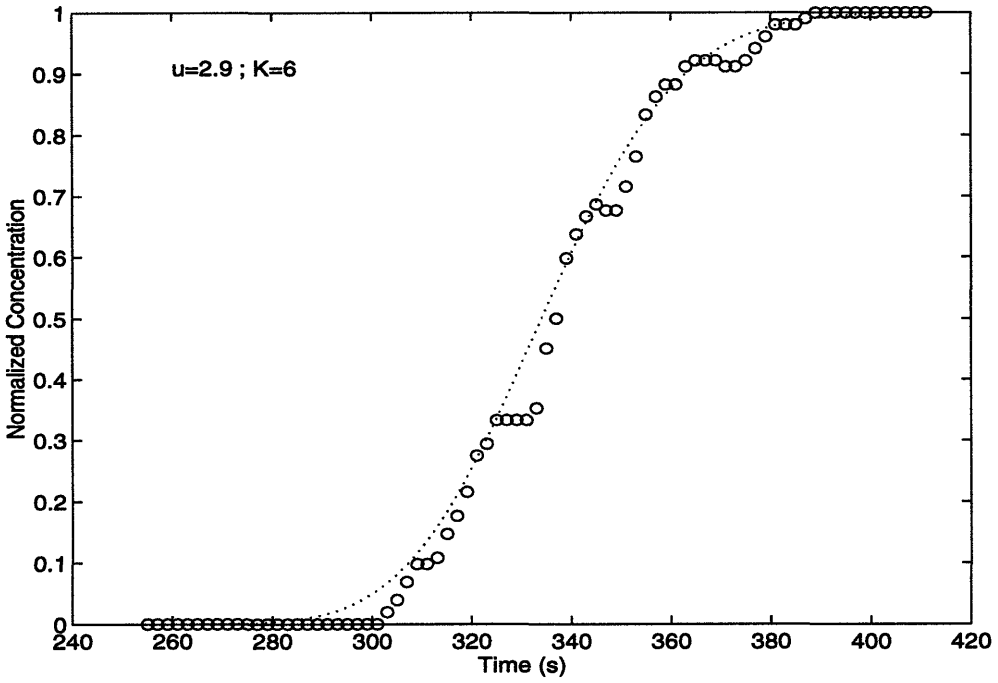

Figure A-1: Least-squared fit (no dowel, low velocity)

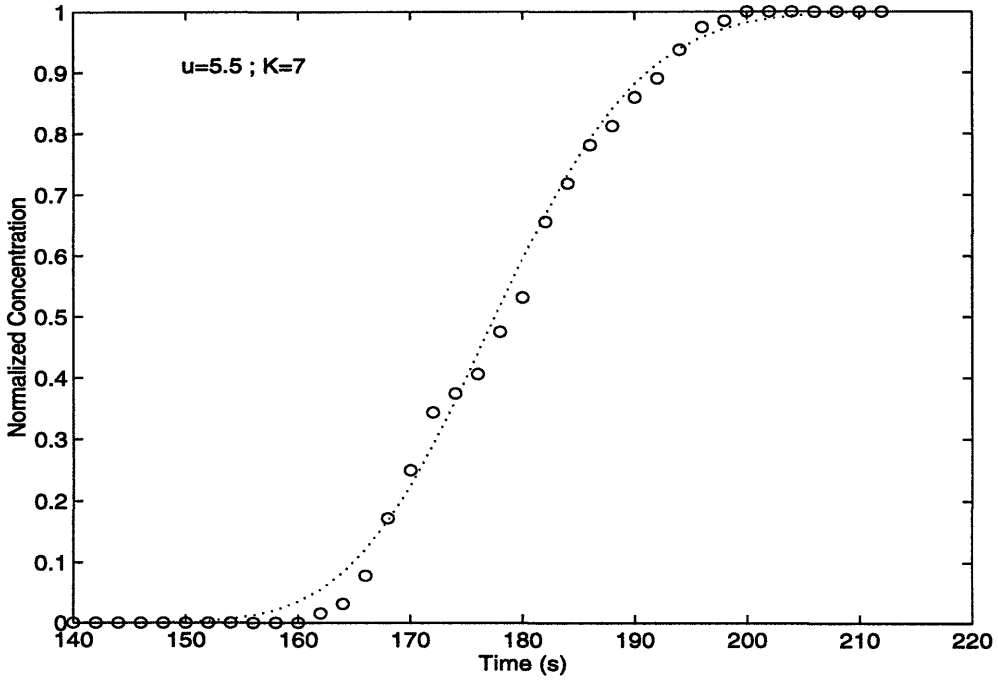

Figure A-2: Least-squared fit (no dowel, medium velocity)

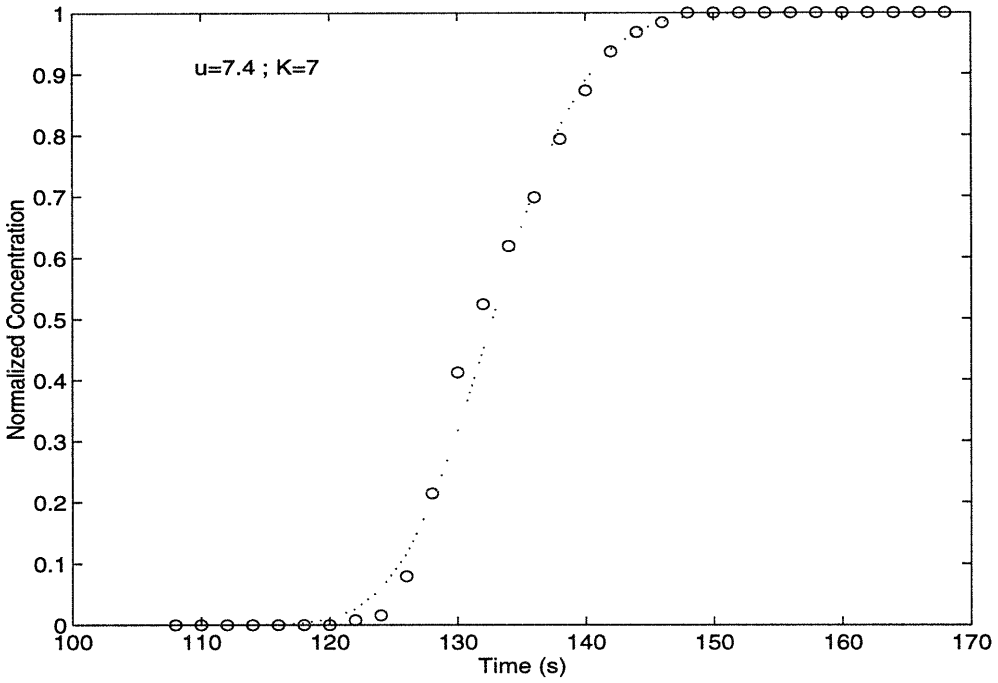

Figure A-3: Least-squared fit (no dowel, high velocity)

Appendix B

Concentration Curves

Dowel Cases

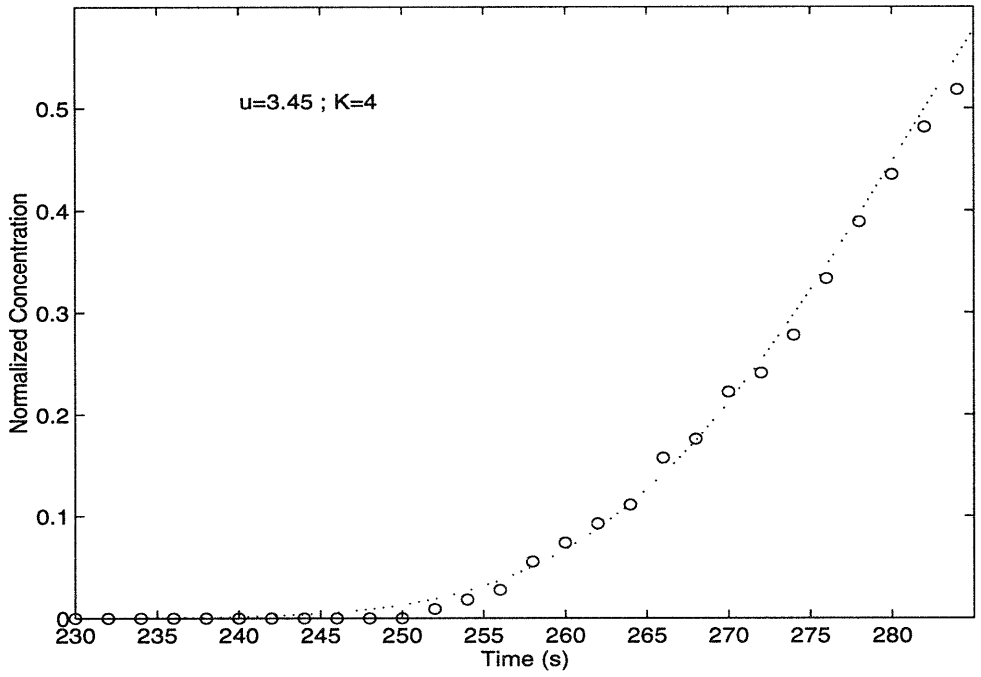

Figure B-1: Least-squared fit (low density, low velocity)

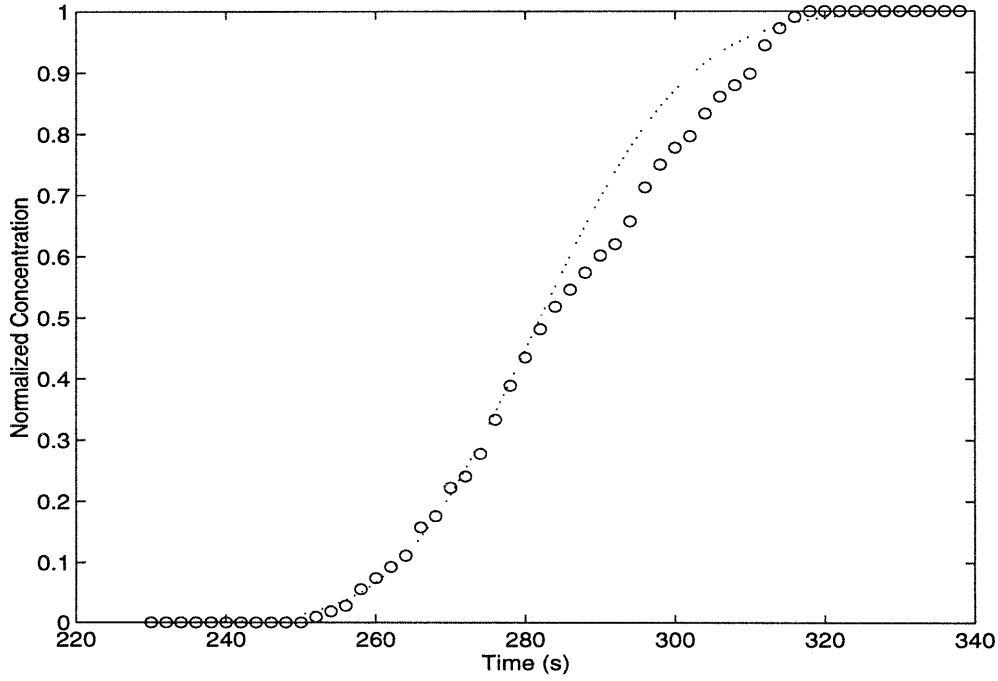

Figure B-2: Observation of delay phenomenon (low density, low velocity)

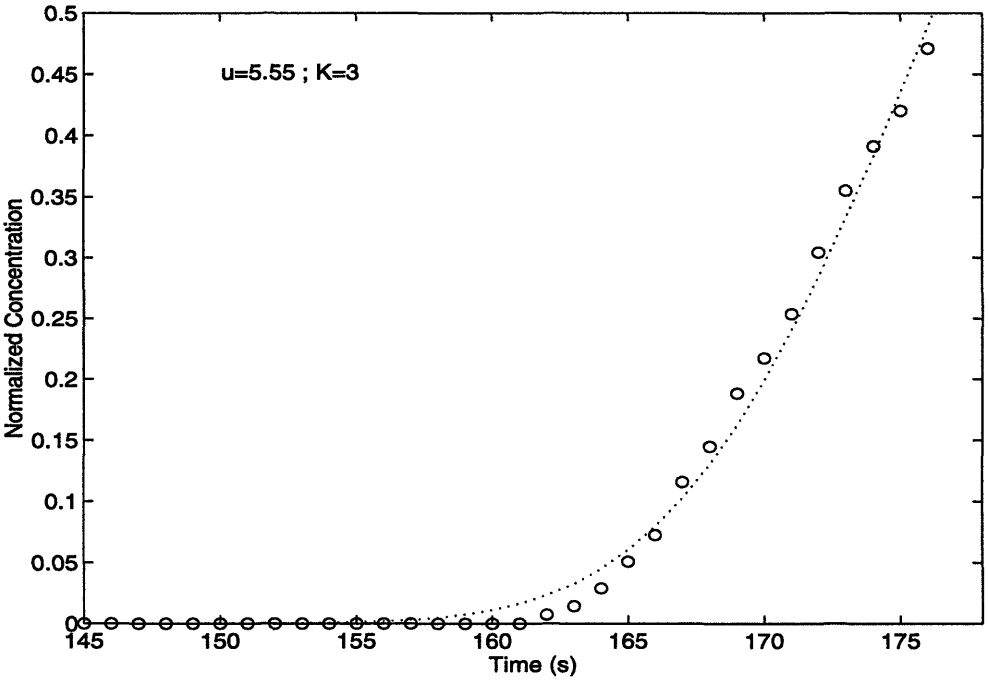

Figure B-3: Least-squared fit (low density, medium velocity)

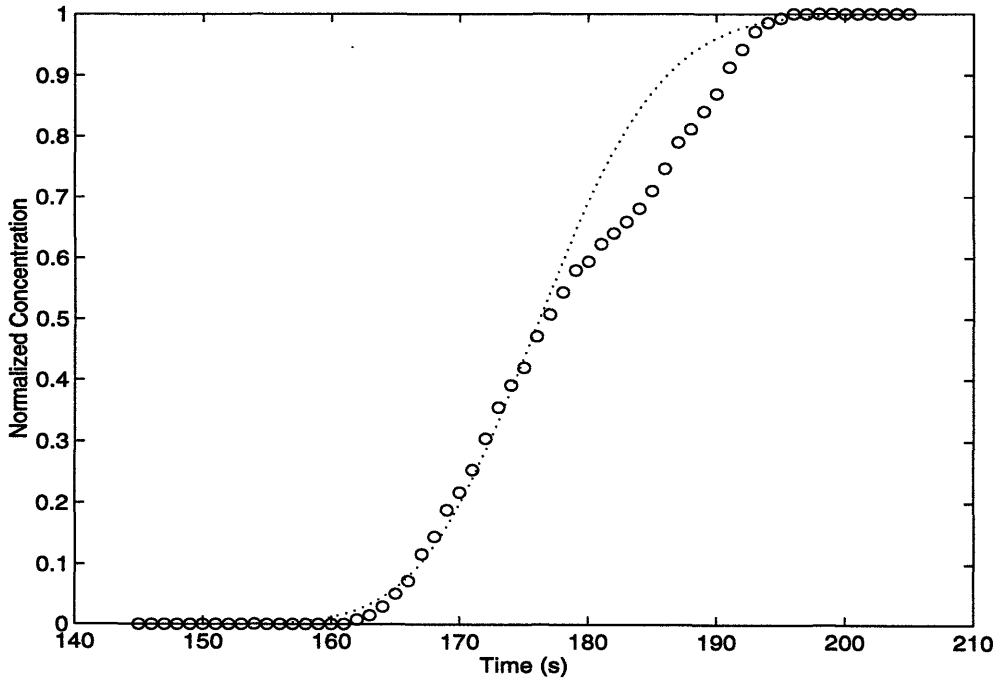

Figure B-4: Observation of delay phenomenon (low density, medium velocity)

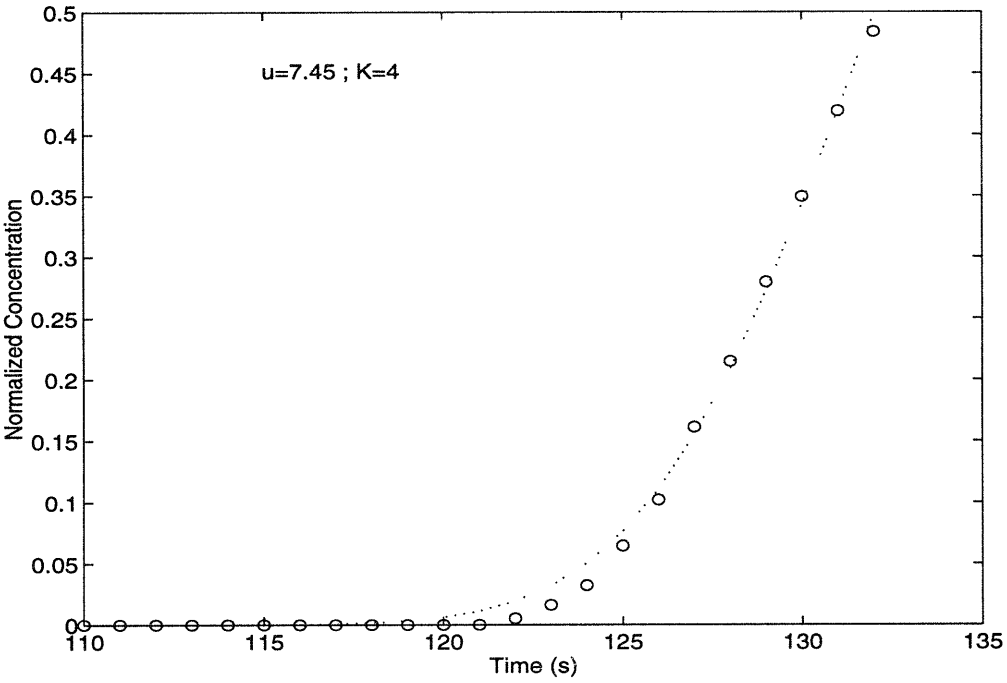

Figure B-5: Least-squared fit (low density, high velocity)

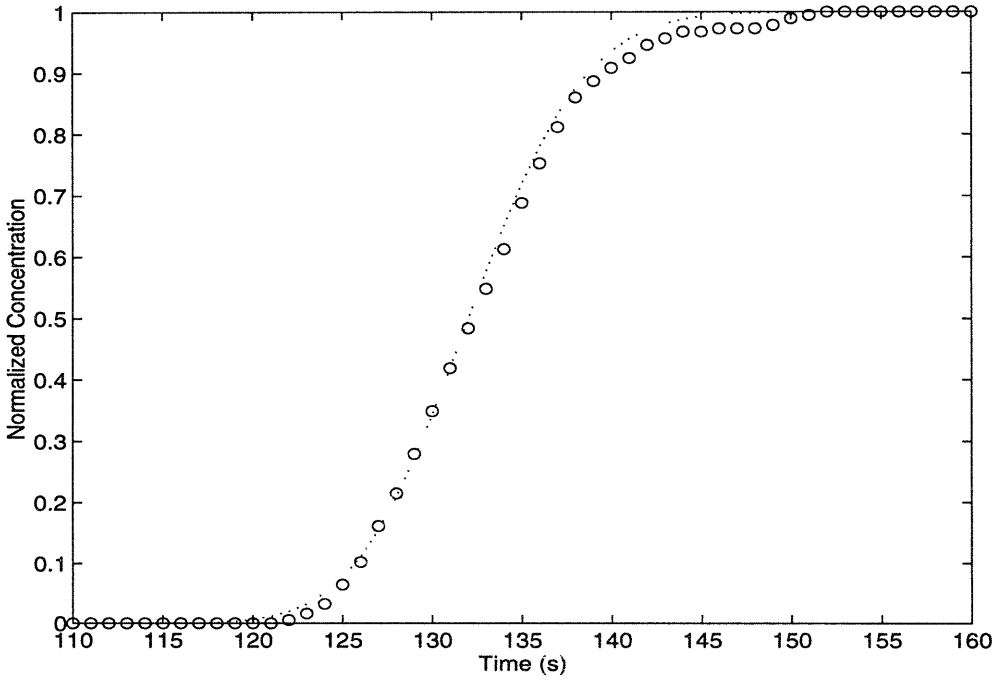

Figure B-6: Observation of delay phenomenon (low density, high velocity)

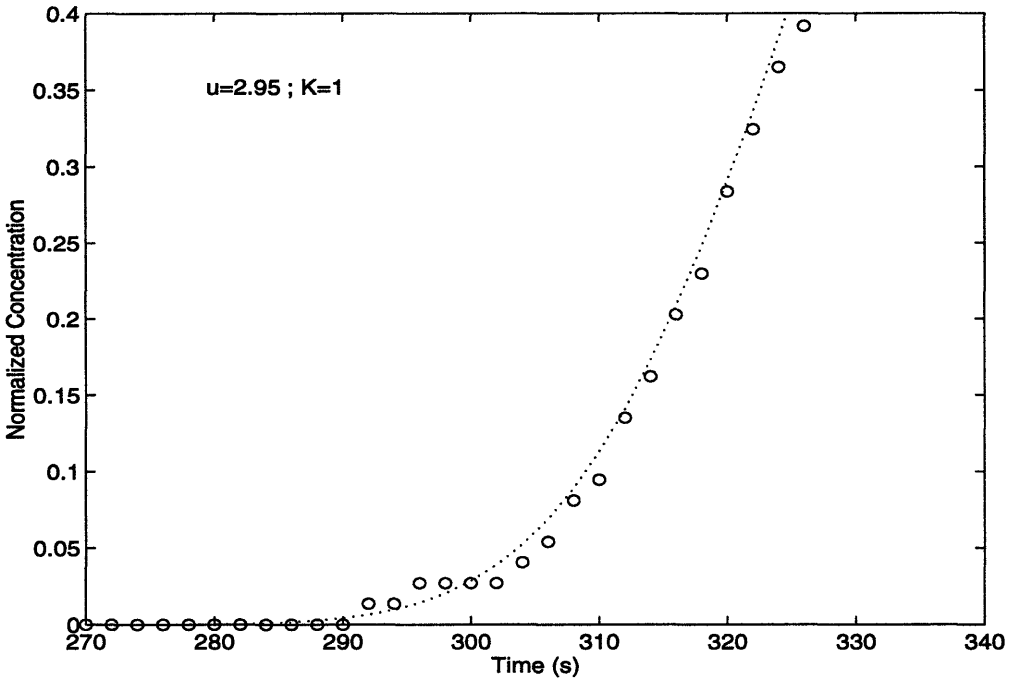

Figure B-7: Least-squared fit (medium density, low velocity)

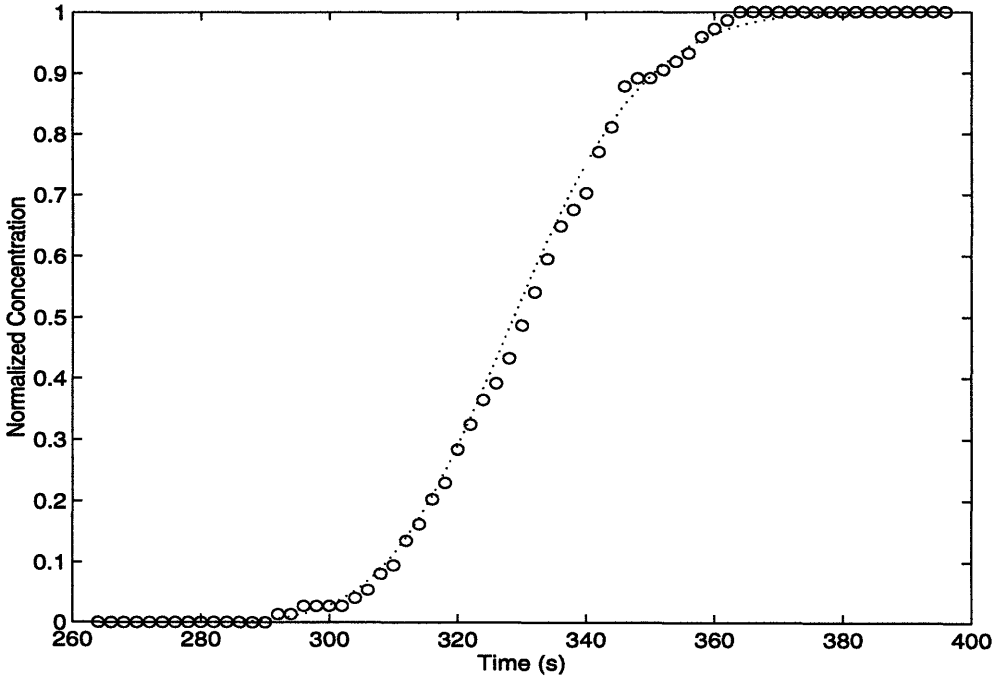

Figure B-8: Observation of delay phenomenon (medium density, low velocity)

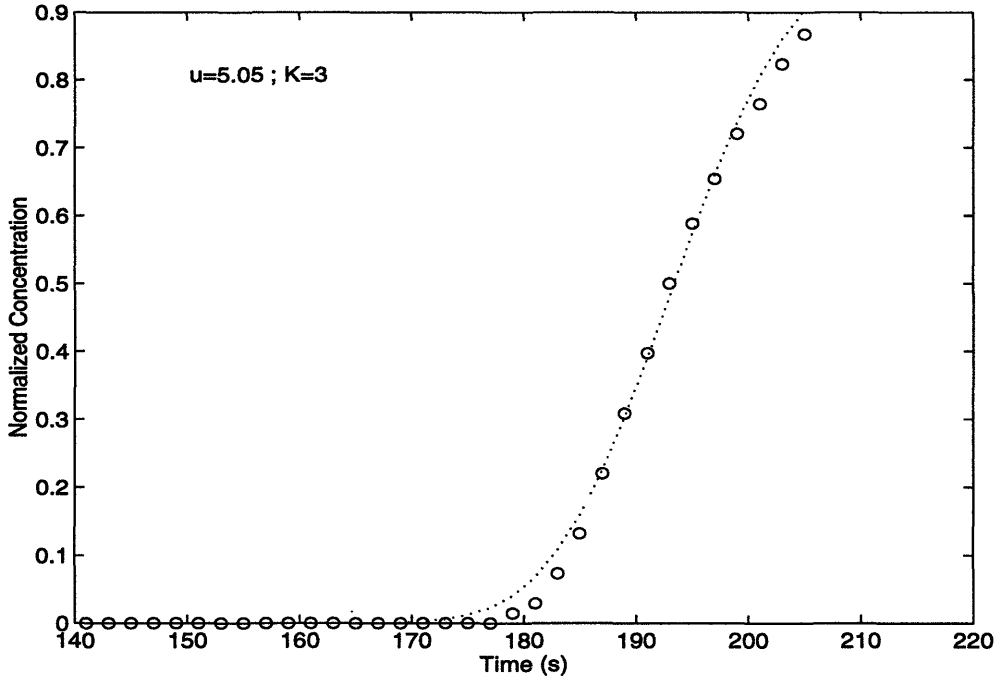

Figure B-9: Least-squared fit (medium density, medium velocity)

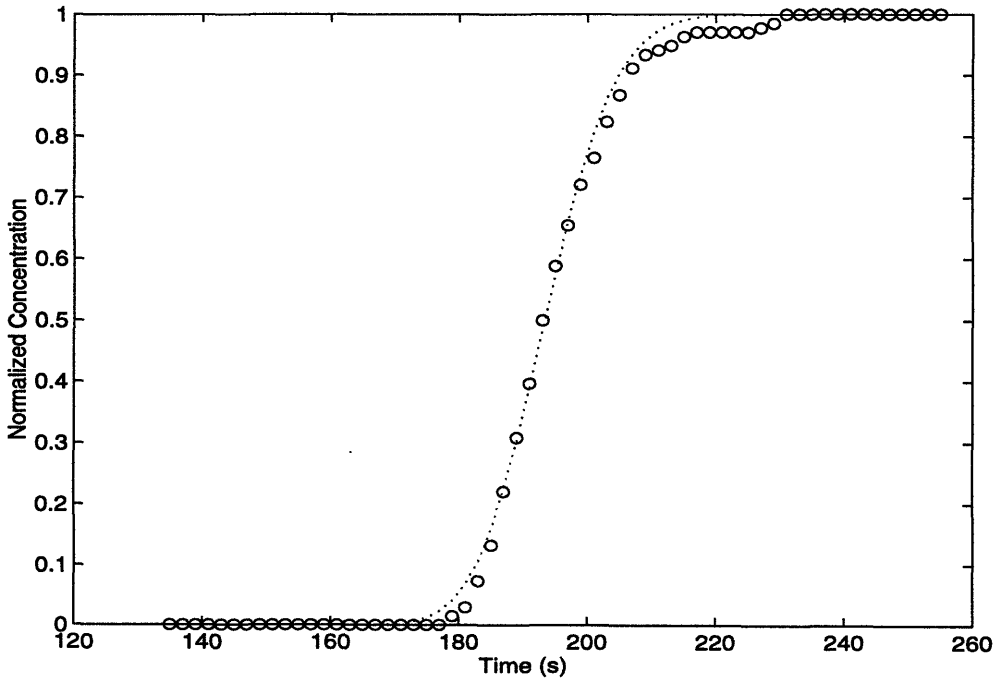

Figure B-10: Observation of delay phenomenon (medium density, medium velocity)

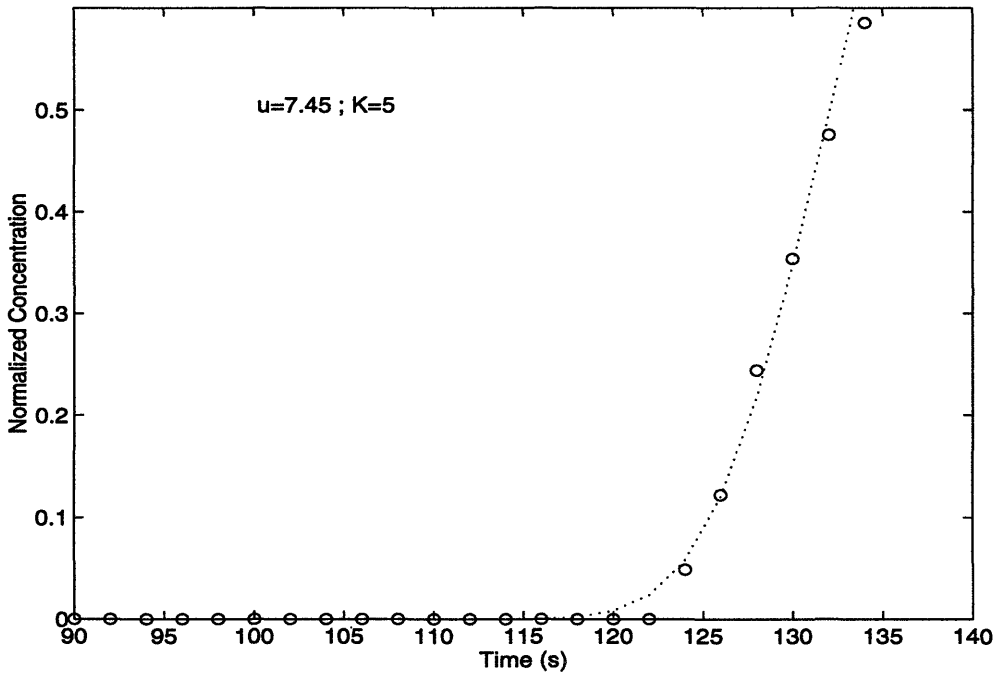

Figure B-11: Least-squared fit (medium density, high velocity)

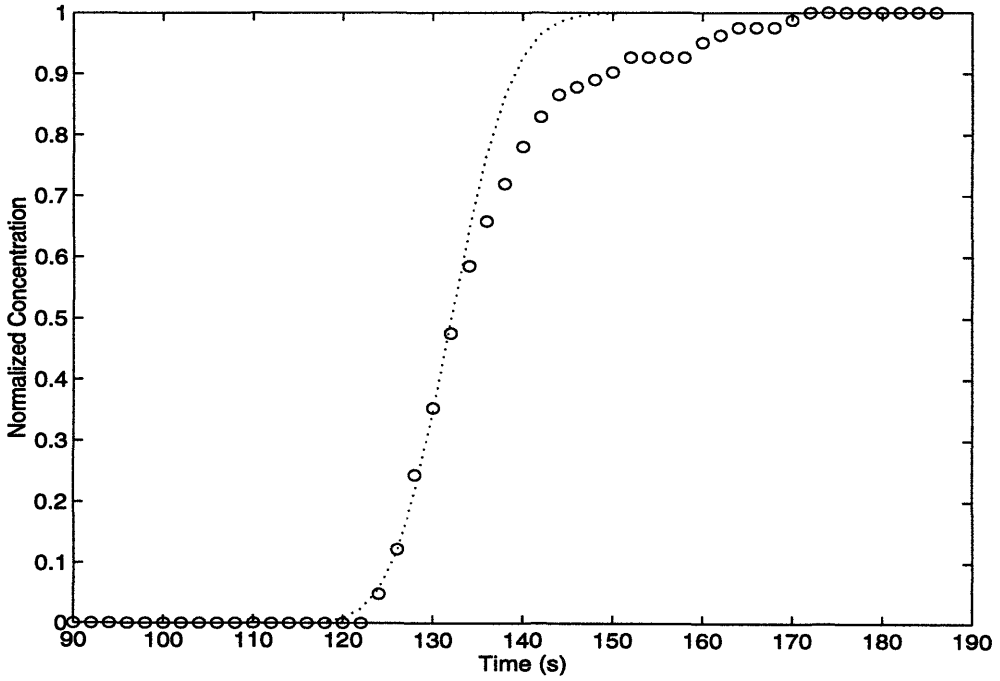

Figure B-12: Observation of delay phenomenon (medium density, high velocity)

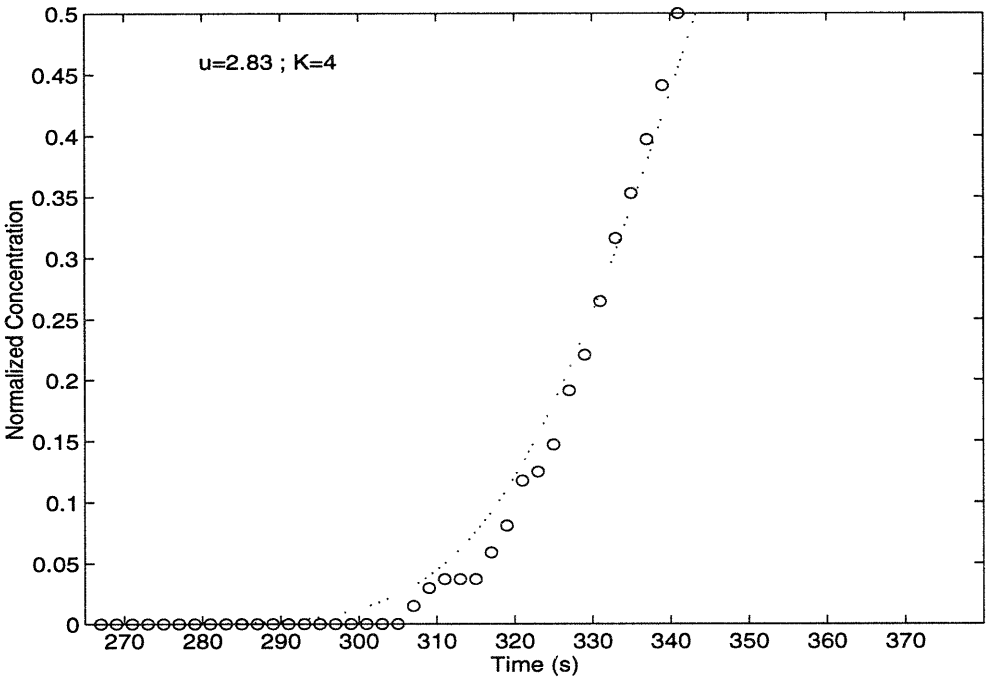

Figure B-13: Least-squared fit (high density, low velocity)

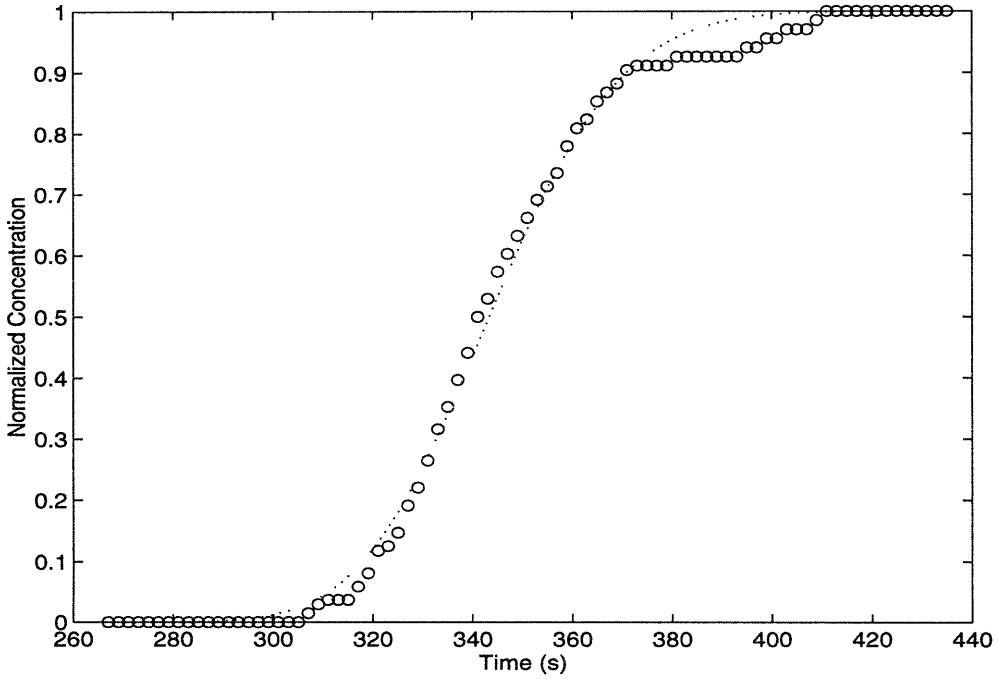

Figure B-14: Observation of delay phenomenon (high density, low velocity)

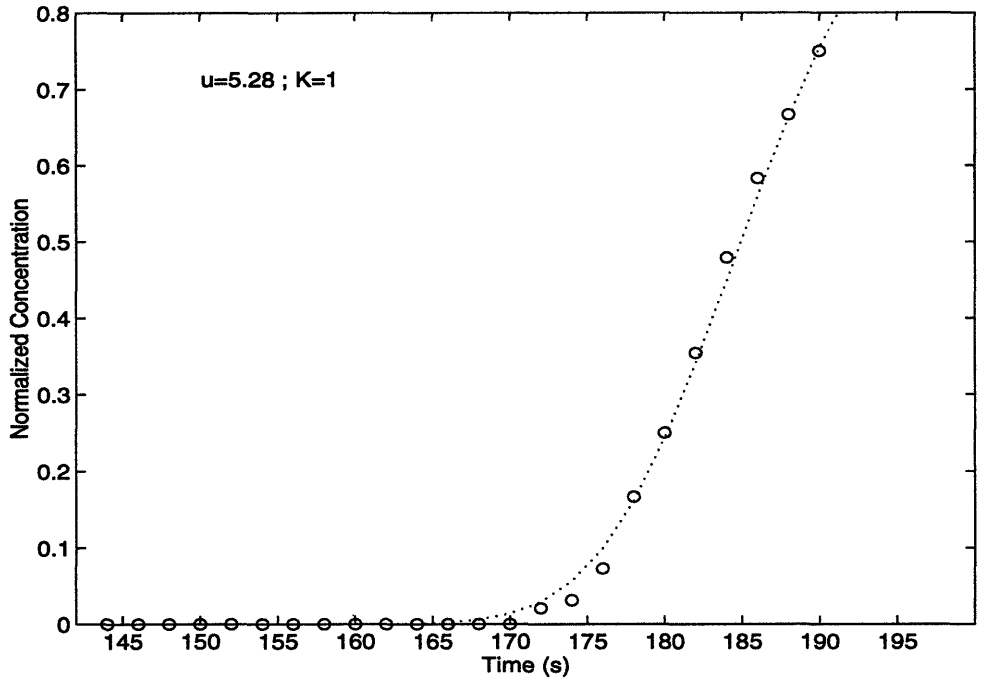

Figure B-15: Least-squared fit (high density, medium velocity)

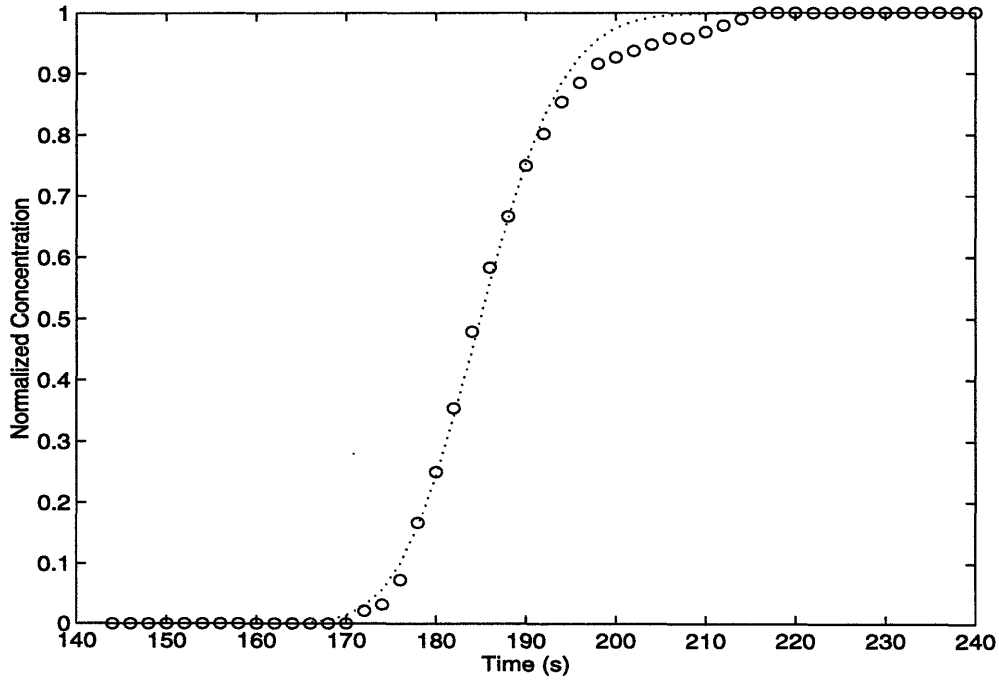

Figure B-16: Observation of delay phenomenon (high density, medium velocity)

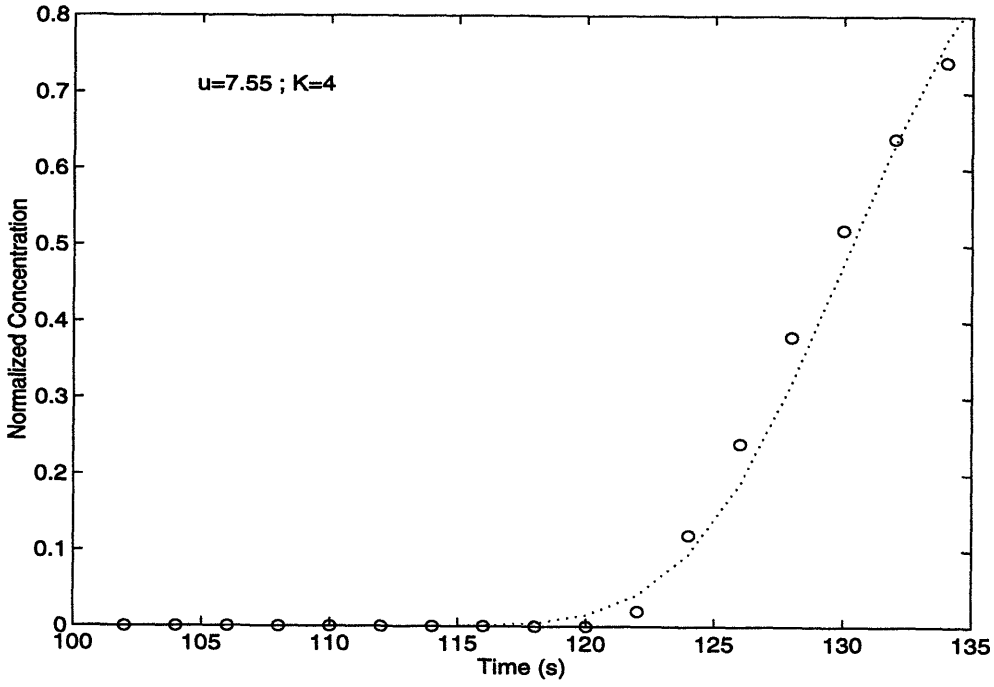

Figure B-17: Least-squared fit (high density, high velocity)

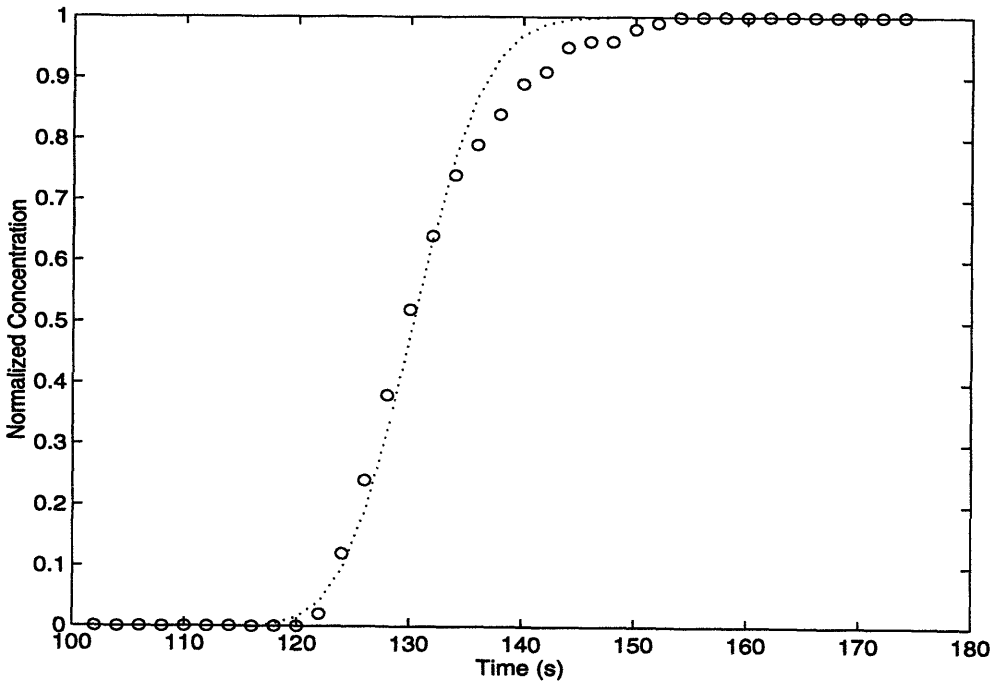

Figure B-18: Observation of delay phenomenon (high density, high velocity)

Appendix C

Listing of Numerical Model

model.m

```
clear;
    density=5;
    d=density/100;
    U=6;
    w=U/5;
    T=round(20/(3*w));          (delay inside a dead-zone)
    h=20;
    dt=1;
    A=d*w/h;
    dx=U*dt;                    (in this case N=1)
    l2=600;
    l1=150;
    M=T/dt;
    L=l2/dx;
    D=l1/dx;
cnt=zeros([1,3*L]);
ct=zeros([M,3*L]);
    for I=1:1:1
        cnt(1,I)=1;             (boundary condition)
    end;
t=dt;
    for I=2:1:2.5*L
        t=t+dt;
        step1
        step2
        stat
        sigma(t)=s;
        mean(t)=m;
    end;
```

step1.m

```
cnt=(cnt+ct(1,:));
   for J=1:1:M-1
      ct(J,:)=ct(J+1,:);              (release process)
   end;
ct(M,:)=zeros([1,3*L]);
```

step2.m

```
   for I=D:1:L-1
      ct(M,I)=A*dt*cnt(1,I);
   end;
   for I=3*L:-1:L+1
      cnt(1,I)=cnt(1,I-1);            (advection and trapping process)
   end;
   for I=L:-1:D+1
      cnt(1,I)=(1-A*dt)*cnt(1,I-1);
   end;
   for I=D:-1:2
      cnt(1,I)=cnt(1,I-1);
   end;
cnt(1,1)=0;
```

stat.m

```
n=length(cnt(1,:));
clear c;
c=zeros([1,n]);
   for I=1:1:M
      c(1,:)=c(1,:)+ct(I,:);
   end;
c(1,:)=c(1,:)+cnt(1,:);
q=0;
   for I=1:1:n
      q=q+c(1,I);                     (computation of total mass)
   end;
m=0;
   for I=1:1:n
      m=m+I*dx*c(1,I);                (computation of center of mass)
   end;
s=0;
   for I=1:1:n
      s=s+(I*dx)^2*c(1,I);            (computation of spatial variance)
   end;
s=sqrt(s-m^2);
```

Bibliography

[1] N. D. Abd El-Hadi and K. S. Davar. Longitudinal dispersion for flow over rough beds. *Journal of the Hydraulics Division*, 102(HY4):483–498, April 1976.

[2] S. C. Chikwendu and G. U. Ojiakor. Slow-zone model for longitudinal dispersion in two-dimensional shear flows. *Journal of Fluid Mechanics*, 152:15–38, 1985.

[3] M. Coutanceau and R. Bouard. Experimental determination of the main features of the viscous flow in the wake of a circular cylinder in uniform translation. part 1. steady flow. *Journal of Fluid Mechanics*, 79(2):231–256, 1977.

[4] J. W. Elder. The dispersion of marked fluid in turbulent shear flow. *Journal of Fluid Mechanics*, 5(4):544–560, 1959.

[5] M. L. Fernald. *Gray's Manual of Botany.* American Book Company, 8^{th} edition, 1950.

[6] H. B. Fischer. The mechanics of dispersion in natural streams. *Journal of the Hydaulics Division*, 93(HY6):187–216, November 1967.

[7] H. B. Fischer. Dispersion predictions in natural streams. *Journal of the Sanitary Engineering Division*, 94(SA5):927–943, October 1968.

[8] H. B. Fischer. *Mixing in Inland and Coastal Waters.* Academic Press, 1979.

[9] G. H. Gerrard. The wakes of cylindrical bluff bodies at low reynolds number. *Philosophical Transactions of the Royal Society of London*, 288A:351–382, 1978.

[10] L. S. G. Kovasznay. Hot-wire investigation of the wake behind cylinders at low reynolds number. *Proceedings of the Royal Society of London*, 198A:174–190, 1949.

[11] C. Legrand-Marcq and H. Laudelout. Longitudinal dispersion in a forest stream. *Journal of Hydrology*, 78:317–324, 1985.

[12] O. Levenspiel and W. K. Smith. Notes on the diffusion-type model for the longitudinal mixing of fluids in flow. *Chemical Engineering Science*, 6:227–233, 1957.

[13] L. MacDonald. Water pollution solution : build a marsh. *American Forests*, 100(7-8):26–29, July 1994.

[14] Managing wastewater in coastal urban areas. National Academy Press, 1993.

[15] M. Nishioka and H. Sato. Measurements of velocity distributions in the wake of a circular cylinder at low reynolds number. *Journal of Fluid Mechanics*, 65(1):97–112, 1974.

[16] C. F. Jr. Nordin and G. V. Sabol. Empirical data on longitudinal dispersion in rivers. U.S. Geological Survey Water-Ressources Investigation Report, 1974.

[17] C. F. Jr. Nordin and B. M. Troutman. Longitudinal dispersion in rivers : The persistence of skewness in observed data. *Water Ressources Research*, 16(1):123–128, February 1980.

[18] H. Schlichting. *Boundary-Layer Theory.* McGraw-Hill, 1968.

[19] I. W. Seo. Laboratory and numerical investigation of longitudinal dispersion in open channels. *Water Ressources Bulletin*, 26(5):811–822, October 1990.

[20] P. L. Smart and I. M. S. Laidlaw. An evaluation of some fluorescent dyes for water tracing. *Water Ressources Research*, 13(1):15–33, February 1977.

[21] H. Tamura, M. Kiya, and M. Arie. Vortex shedding from a circular cylinder in moderate-reynolds-number shear flow. *Journal of Fluid Mechanics*, 141(4):721–735, 1980.

[22] G. I. Taylor. Dispersion of soluble matter in solvent flowing slowly through a tube. *Proceedings Royal Society London*, 223A:446–468, 1954.

[23] E. M. Valentine and I. R. Wood. Longitudinal dispersion with dead zones. *Journals of the Hydraulics Division*, 103(HY9):975–990, sept 1977.

[24] Y. Yu and L. Wenzhi. Longitudinal dispersion in rivers : a dead-zone model solution. *Water Ressources Bulletin*, 25(2), April 1989.

[25] Rebecca Anne Zavistoski. Hydrodynamic effects of surface piercing plants. Master's project, Massachusetts Institute of Technology, Civil and Environmental Engineering Department, sept 1994.